Chapter 17
Related Techniques

Concepts and techniques similar to those used in radio interferometry and synthesis imaging occur in various areas of astronomy, Earth remote sensing, and space science. Here we introduce a few of them, including optical techniques, to leave the reader with a broader view. All of these subjects are described in detail elsewhere, so here the aim is mainly to outline the principles involved and to make connections between them and the material developed in earlier chapters.

17.1 Intensity Interferometer

In long-baseline interferometry, the intensity interferometer offers some technical simplifications that were mainly of importance in radio astronomy during the early development of the subject. As mentioned in Sect. 1.3.7, its practical applications in radio astronomy have been limited (Jennison and Das Gupta 1956; Carr et al. 1970; Dulk 1970) because, in comparison with a conventional interferometer, an intensity interferometer requires a much higher signal-to-noise ratio (SNR) in the receiving system, and only the modulus of the visibility function is measured. This type of interferometer was devised by Hanbury Brown, who has described its development and application (Hanbury Brown 1974).

In the intensity interferometer, the signals from the antennas are amplified and then passed through square-law (power-linear) detectors before being applied to a correlator, as shown in Fig. 17.1. As a result, the rms signal voltages at the correlator inputs are proportional to the powers delivered by the antennas and therefore also proportional to the intensity of the signal. No fringes are formed because the phase of the radio frequency (RF) signals is lost in the detection, but the correlator output indicates the degree of correlation of the detected waveforms. Let the voltages at the detector inputs be V_1 and V_2. The outputs of the detectors are V_1^2 and V_2^2 and

A.R. Thompson, J.M. Moran, and G.W. Swenson Jr., *Interferometry and Synthesis in Radio Astronomy*, Astronomy and Astrophysics Library,
DOI 10.1007/978-3-319-44431-4_17

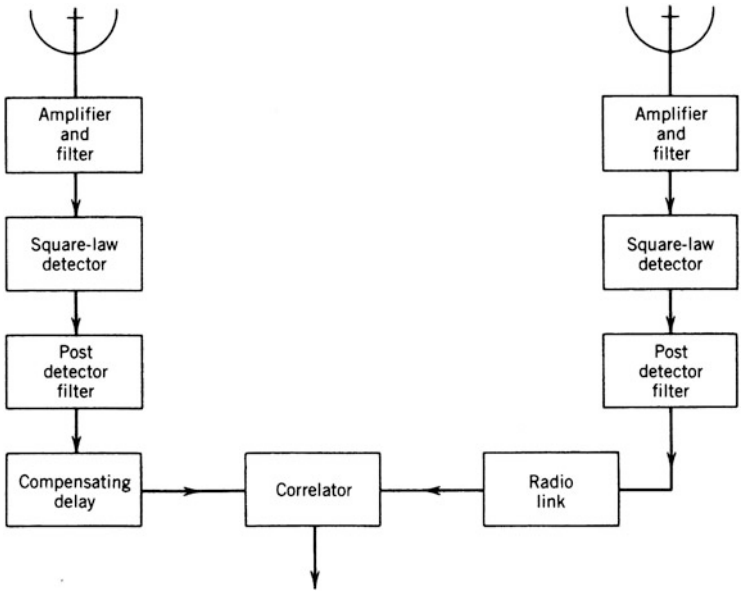

Fig. 17.1 The intensity interferometer. The amplifier and filter block may also incorporate a local oscillator and mixer. The compensating delay equalizes the time delays of signals from the source to the correlator inputs. The post-detector filters remove dc and radio frequency components.

each consists of a dc component, which is removed by a filter, and a time-varying component, which goes to an input of the correlator. From the fourth-order moment relation [Eq. (6.36)], the correlator output is

$$\begin{aligned}\left\langle (V_1^2 - \langle V_1^2 \rangle)(V_2^2 - \langle V_2^2 \rangle) \right\rangle &= \langle V_1^2 V_2^2 \rangle - \langle V_1^2 \rangle \langle V_2^2 \rangle \\ &= 2\langle V_1 V_2 \rangle^2 \, . \end{aligned} \tag{17.1}$$

The correlator output is proportional to the square of the correlator output for a conventional interferometer and measures the squared modulus of the visibility of a source under observation.

We now give an alternative derivation of the response, which provides a physical picture of how the signals from different parts of the source combine within the instrument. The source is represented as a one-dimensional intensity distribution in Fig. 17.2. We suppose that it can be considered as a linear distribution of many small regions, each of which is large enough to emit a signal with the characteristics of stationary random noise, but of angular width small compared with $1/u$, which defines the angular resolution of the interferometer. The source is assumed to be spatially incoherent so the signals from different regions are uncorrelated. Consider two regions of the source, k and ℓ, at angular positions θ_k and θ_ℓ and subtending

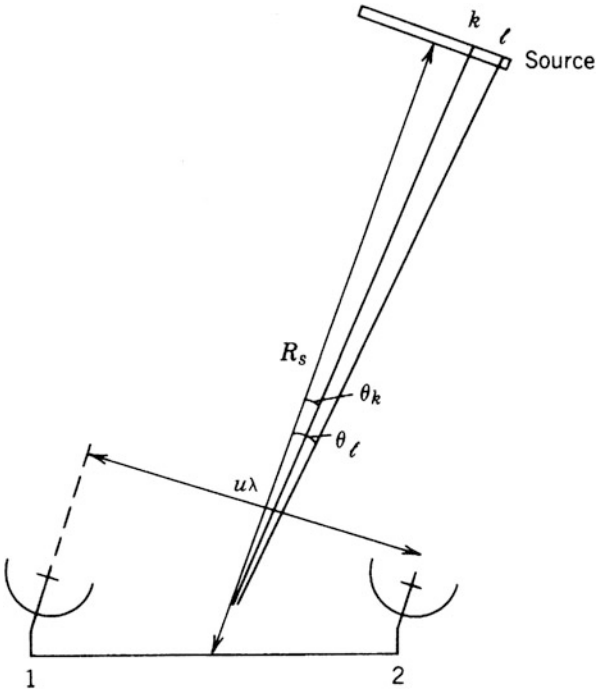

Fig. 17.2 Distances and angles used in the discussion of the intensity interferometer. u is the projected antenna spacing in wavelengths.

angles $d\theta_k$ and $d\theta_\ell$, as in Fig. 17.2. Each radiates a broad spectrum, but we first consider only the output resulting from a Fourier component at frequency ν_k from region k and similarly a component at ν_ℓ from region ℓ. Let $A_1(\theta)$ be the power reception pattern of the two antennas and $I_1(\theta)$ the intensity distribution of the source, these two functions being one-dimensional representations. Then the detector output of the first receiver is equal to

$$[V_k \cos 2\pi \nu_k t + V_\ell \cos(2\pi \nu_\ell t + \phi_1)]^2 \ , \tag{17.2}$$

where ϕ_1 is a phase term resulting from path-length differences, and the signal voltages V_k and V_ℓ are given by

$$V_k^2 = A_1(\theta_k) I_1(\theta_k)\, d\theta_k\, d\nu_k \tag{17.3}$$

and

$$V_\ell^2 = A_1(\theta_\ell) I_1(\theta_\ell)\, d\theta_\ell\, d\nu_\ell \ . \tag{17.4}$$

After expanding (17.2) and removing the dc and RF terms, we obtain for the detector output from receiver 1:

$$V_k V_\ell \cos\left[2\pi(\nu_k - \nu_\ell)t - \phi_1\right] \ . \tag{17.5}$$

Similarly, the detector output from receiver 2 is

$$V_k V_\ell \cos\left[2\pi(\nu_k - \nu_\ell)t - \phi_2\right] \ . \tag{17.6}$$

The correlator output is proportional to the time-averaged product of (17.5) and (17.6), that is, to

$$\langle A_1(\theta_k)A_1(\theta_\ell)I_1(\theta_k)I_1(\theta_\ell)\, d\theta_k\, d\theta_\ell\, d\nu_k\, d\nu_\ell\, \cos(\phi_1 - \phi_2)\rangle \ . \tag{17.7}$$

The change in the phase term with respect to frequency is small so long as the fractional bandwidth is much less than the ratio of the resolution to the field of view [see Eq. (6.69) and related discussion]. With this restriction, expression (17.7) is effectively independent of the frequencies ν_k and ν_ℓ, so that if we integrate it with respect to ν_k and ν_ℓ over a rectangular receiving passband of width $\Delta\nu$, $d\nu_k\, d\nu_\ell$ is replaced by $\Delta\nu^2$.

The phase angles ϕ_1 and ϕ_2 result from the path differences kk' and $\ell\ell'$ shown in Fig. 17.3. Note that ϕ_1 and ϕ_2 have opposite signs since the excess path length to antenna 1 is from point ℓ and that to antenna 2 is from point k. If R_s is the distance of the sources from the antennas, the distance $k\ell$ in the source is approximately equal to $R_s(\theta_k - \theta_\ell)$. The angle $\alpha_k + \alpha_\ell$ is approximately equal to $u\lambda/R_s$, since u represents the antenna spacing projected normal to the source and measured in wavelengths. The preceding approximations are accurate if α_k, α_ℓ, and the angle subtended by the source are all small. Thus, the difference of the phase angles is

$$\begin{aligned} \phi_1 - \phi_2 &= 2\pi R_s(\theta_k - \theta_\ell)\frac{(\sin\alpha_k + \sin\alpha_\ell)}{\lambda} \\ &\simeq 2\pi u(\theta_k - \theta_\ell) \ . \end{aligned} \tag{17.8}$$

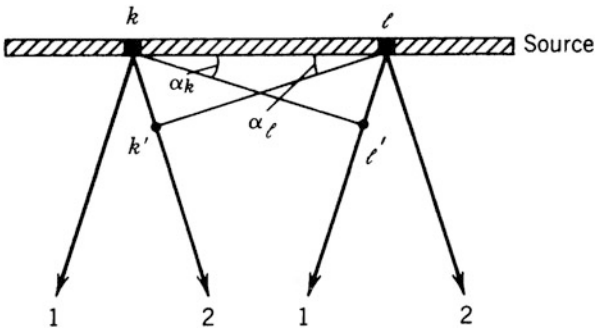

Fig. 17.3 Relative delay paths kk' and $\ell\ell'$ from regions k and ℓ of the source for rays traveling in the directions of antennas 1 and 2.

From (17.7), the output of the correlator now becomes

$$\left\langle A_1(\theta_k)A_1(\theta_\ell)I_1(\theta_k)I_1(\theta_\ell)\Delta\nu^2\cos\left[2\pi u(\theta_k-\theta_\ell)\right]d\theta_k\,d\theta_\ell\right\rangle\ . \tag{17.9}$$

To obtain the output from all pairs of regions within the source, expression (17.9) can, with the assumption of spatial incoherence, be integrated with respect to θ_k and θ_ℓ over the source, giving

$$\begin{aligned}&\left\langle\left[\Delta\nu\int A_1(\theta_k)I_1(\theta_k)\cos(2\pi u\theta_k)d\theta_k\right]\left[\Delta\nu\int A_1(\theta_\ell)I_1(\theta_\ell)\cos(2\pi u\theta_\ell)d\theta_\ell\right]\right.\\&\left.+\left[\Delta\nu\int A_1(\theta_k)I_1(\theta_k)\sin(2\pi u\theta_k)d\theta_k\right]\left[\Delta\nu\int A_1(\theta_\ell)I_1(\theta_\ell)\sin(2\pi u\theta_\ell)d\theta_\ell\right]\right\rangle\\&=A_0^2\Delta\nu^2\left[\mathcal{V}_\mathrm{R}^2+\mathcal{V}_\mathrm{I}^2\right]=A_0^2\Delta\nu^2\left|\mathcal{V}\right|^2\ ,\end{aligned} \tag{17.10}$$

where we assume that the antenna response $A_1(\theta)$ has a constant value A_0 over the source, and the subscripts R and I denote the real and imaginary parts of the visibility. This result follows from the definition of visibility that is given for a two-dimensional source in Sect. 3.1.1. Thus, the correlator output is proportional to the square of the modulus of the complex visibility. For a more detailed discussion following the same approach, see Hanbury Brown and Twiss (1954). An analysis based on the mutual coherence of the radiation field is given by Bracewell (1958).

Some characteristics of the intensity interferometer offer advantages over the conventional interferometer. The intensity interferometer is much less sensitive to atmospheric phase fluctuations, because each signal component at the correlator input is generated as the difference between two radio frequency components that have followed almost the same path through the atmosphere. The phase fluctuations in the difference-frequency components at the detectors are less than those in the radio frequency signals by the ratio of the difference frequency to the radio frequency, which may be of order 10^{-5}. In the conventional interferometer, such phase fluctuations can make the amplitude, as well as the phase, of the visibility difficult to measure. Similarly, fluctuations in the phases of the local oscillators in the two receivers do not contribute to the phases of the difference-frequency components. Thus, it is not necessary to synchronize the local oscillators or even to use high-stability frequency standards, as in VLBI. These advantages were helpful, although by no means essential, in the early radio implementation of the intensity interferometer. Had the diameters of the sources under investigation then been of order of arcseconds, rather than arcminutes, the characteristics of the intensity interferometer would have played a more essential role.

The serious disadvantage of the intensity interferometer is its relative lack of sensitivity. Because of the action of the detectors in the receivers, the ratio of the signal power to the noise power at the correlator inputs is proportional to the square of the corresponding ratio in the RF (predetector) stages, the exact value being dependent on the bandwidths of these and the post-detector stages (Hanbury Brown and Twiss 1954). In a conventional interferometer, it is possible to detect signals that

are $\sim$ 60 dB below the noise at the correlator inputs. In the intensity interferometer, a similar SNR at the correlator output would require SNRs greater by $\sim$ 30 dB in the RF stages. This effect, together with the lack of sensitivity to the visibility phase, has greatly restricted the radio usage of the intensity interferometer. Intensity interferometry played a similar role in the early days of optical interferometry (see Sect. 17.6.3) before the development of the modern Michelson interferometer.

17.2 Lunar Occultation Observations

Measurement of the light intensity from a star as a function of time during occultation by the Moon was suggested by MacMahon (1909) as a means of determining the star's size and position. His analysis, which was based on a simple consideration of geometric optics, was criticized by Eddington (1909), who stated that diffraction effects would mask the detail at the angular scale of the star. Eddington's paper probably discouraged observations of lunar occultations for some time. The first occultation measurements were reported 30 years later by Whitford (1939), who observed the stars β Capricorni and ν Aquarii and obtained clear diffraction patterns.

What was not realized by Eddington and others at the time was that although the temporal response to an occultation is not a simple step function, as it would be for the case of geometrical optics and a point source, the Fourier transform of the point-source response, which represents the sensitivity to spatial frequency on the sky, has the same amplitude as that of a step function and differs only in the phase. Hence, the lunar occultation is sensitive to all Fourier components, and there is no intrinsic limit to the resolution that can be obtained, except for that imposed by the finite SNR. This equality of the amplitudes was recognized by Scheuer (1962), who devised a method of deriving the one-dimensional intensity distribution I_1 from the occultation curve. By that time, the concept of spatial frequency had become widely understood through application to radio interferometry. Since, in lunar occultations, the diffraction occurs outside the Earth's atmosphere, the high angular resolution is not corrupted significantly by atmospheric effects, as it is in the case of ground-based interferometry. Furthermore, the only dependence of the obtainable resolution on the telescope size results from the SNR. An early radio application of the technique was the measurement of the position and size of 3C273 by Hazard et al. (1963), which led to the identification of quasars. As mentioned in Sect. 12.1, this position measurement was used for many years as the right ascension reference for VLBI position catalogs. Radio occultation measurements have been most important at meter wavelengths, since at shorter wavelengths, the high thermal flux density from the Moon presents a difficulty. At radio frequencies, lunar occultations have been largely superseded by interferometry, but lunar occultations are still useful at optical and infrared wavelengths.

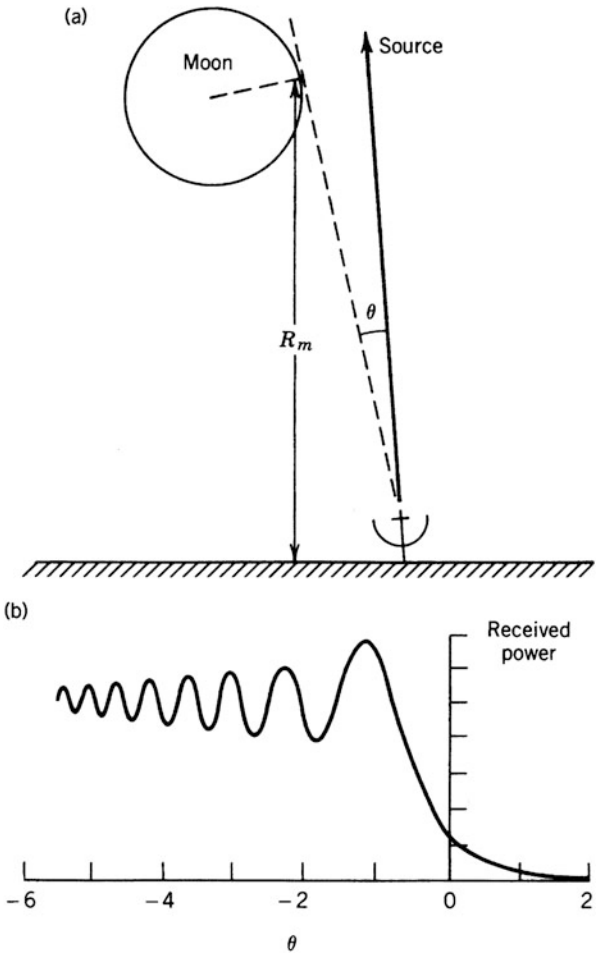

Fig. 17.4 Occultation of a radio source by the Moon: (**a**) the geometrical situation, in which θ is measured clockwise from the direction of the source, and is negative as shown; (**b**) the occultation curve for a point source, which is proportional to $\mathcal{P}(\theta)$. The units of θ on the abscissa are equal to $\sqrt{\lambda/2R_m}$, where λ is the wavelength and R_m the Moon's distance.

Figure 17.4 shows the geometrical situation and the form of an occultation record. The departure of the Moon's limb from a straight edge, as a result of curvature and roughness, is small compared with the size of the first Fresnel zone at radio frequencies. Thus, the point-source response is the well-known diffraction pattern of a straight edge, which is derived in most texts on physical optics. The main change in the received power in Fig. 17.4b corresponds to the covering or uncovering of the first Fresnel zone by the Moon, and the oscillations result from higher-order zones. The critical scale is the size of the first Fresnel zone, $\sqrt{(\lambda R_m/2)}$, where $R_m \simeq 3.84\times10^5$ km is the Earth–Moon distance. This corresponds to 4400 m

at 10-cm wavelength and 10 m at 0.5 μm, or 2.3″ and 5 mas, respectively, in angle as seen from the Earth. The maximum velocity of the occulting edge of the Moon is approximately 1 km s^{-1}, but the effective velocity depends on the position of the occultation on the Moon's limb, and we use 0.6 km s^{-1} as a typical figure. Thus, the coverage time of the first Fresnel zone, which determines the characteristic fall time and oscillation period, is typically about 7 s at a wavelength of 10 cm and 16 ms at 0.5 μm.

In the case of the hypothetical geometrical-optics occultation, the observed curve would be the integral of I_1 as a function of θ, the angle between the source and the Moon's limb as in Fig. 17.4a. Then I_1 could be obtained by differentiation. In the actual case, the observed occultation curve $\mathcal{G}(\theta)$ is equal to convolution of $I_1(\theta)$ with the point-source diffraction pattern of the Moon's limb $\mathcal{P}(\theta)$. This convolution is $I_1(\theta) * \mathcal{P}(\theta)$. Differentiation with respect to θ yields

$$\mathcal{G}'(\theta) = I_1(\theta) * \mathcal{P}'(\theta) \ , \tag{17.11}$$

where the primes indicate derivatives. Fourier transformation of the two sides of Eq. (17.11) gives

$$\overline{\mathcal{G}'}(u) = \overline{I}_1(u)\,\overline{\mathcal{P}'}(u) \ , \tag{17.12}$$

where the bar indicates the Fourier transform, the prime indicates a derivative in the θ domain, and u is the conjugate variable of θ.

Now in the geometrical-optics case, $\mathcal{P}(\theta)$ would be a step function, and thus $\mathcal{P}'(\theta)$ would be a delta function for which the Fourier transform is a constant. For the diffraction-limited case, the function $\overline{\mathcal{P}}(u)$ [adapted from Cohen (1969)] is given by

$$\overline{\mathcal{P}}(u) = \frac{j}{u} \exp\left[j2\pi\theta_F^2 u^2 \operatorname{sgn} u\right] \ , \tag{17.13}$$

where θ_F is the angular size of the first Fresnel zone, $\sqrt{\lambda/2R_m}$, and sgn is the sign function, which takes values ± 1 to indicate the sign of u. It follows from the derivative theorem of Fourier transforms that $\overline{\mathcal{P}'}(u) = j2\pi\overline{\mathcal{P}}(u)$, which has a constant amplitude with no zeros and can be divided out from Eq. (17.12). Thus, $I_1(\theta)$ is equal to $\mathcal{G}'(\theta)$ convolved with a function whose Fourier transform is $1/\overline{\mathcal{P}'}(u)$. Scheuer (1962) shows that this last function is proportional to $\mathcal{P}'(-\theta)$, which can be used as a restoring function as follows:

$$\begin{aligned} I_1(\theta) &= \mathcal{G}'(\theta) * \mathcal{P}'(-\theta) \\ &= \mathcal{G}(\theta) * \mathcal{P}''(-\theta) \ . \end{aligned} \tag{17.14}$$

The second form on the right side is more useful since it avoids the practical difficulty of differentiating a noisy occultation curve. In principle, this restoration

provides I_1 without limit on the angular resolution, in contrast with the performance of an array. Remember, however, that the amplitude of the spatial frequency sensitivity of the occultation curve, which is given by Eq. (17.13), is proportional to $1/u$. Thus, in the restoration in Eq. (17.14), the amplitudes of the Fourier components, which also include the noise, are increased in proportion to u. The increase of the noise sets a limit to the useful resolution. This limit can be conveniently introduced by replacing $\mathcal{P}''(\theta)$ in Eq. (17.14) by $\mathcal{P}''(\theta)$ convolved with a Gaussian function of θ θ with a resolution $\Delta\theta$. One then derives I_1 as it would be observed with a beam of the same Gaussian shape. In practice, the introduction of the Gaussian function is essential to the method, since it ensures the convergence of the convolution integral in Eq. (17.14). The optimal choice of $\Delta\theta$ depends on the SNR. Examples of restoring functions for various resolutions can be found in von Hoerner (1964).

The discussion above follows the classical approach to reduction of Moon-occultation observations, which developed from the geometrical optics analogy. One can envisage the reduction more succinctly as taking the Fourier transform of the occultation curve, dividing by $\overline{\mathcal{P}}(u)$ (with suitable weighting to control the increase of the noise), and retransforming to the θ domain. This process is mathematically equivalent to that in Eq. (17.14).

An estimate of the noise-imposed limit on the angular resolution can be obtained using the geometrical optics model, since the SNRs of the Fourier components are the same as for the actual point-source response. Consider the region of an occultation curve (see Fig. 17.4b) in which the main change in the received power occurs, and let τ be a time interval in which the change in the record level is equal to the rms noise. Then if v_m is the rate of angular motion of the Moon's limb over the radio source, the obtainable angular resolution is approximately

$$\Delta\theta = v_\mathrm{m}\tau \ . \tag{17.15}$$

During the interval τ, the flux density at the antenna changes by ΔS. Let θ_s be the width of the main structure of the source in a direction normal to the Moon's limb, and let S be the total flux density of the source. Then for a source of approximately similar dimension in any direction, the average intensity is approximately S/θ_s^2. The change in solid angle of the covered part of the source in time τ is $\theta_s\Delta\theta$, and

$$\frac{\Delta\theta}{\theta_s} \simeq \frac{\Delta S}{S} \ . \tag{17.16}$$

The SNR at the receiver output for a component of flux density ΔS is

$$\mathcal{R}_\mathrm{sn} = \frac{A\Delta S\sqrt{\Delta\nu\tau}}{2kT_S} \ , \tag{17.17}$$

where A is the collecting area of the antenna, $\Delta\nu$ and T_S are the bandwidth and system temperature of the receiving system, and k is Boltzmann's constant. Note that the thermal contribution from the Moon can contribute substantially to T_S. The

conditions that we are considering correspond to $\mathcal{R}_{\rm sn} \simeq 1$, and from Eqs. (17.15)–(17.17), we obtain

$$\Delta\theta = \left(\frac{2kT_S\theta_s}{AS}\right)^{2/3} \left(\frac{v_{\rm m}}{\Delta\nu}\right)^{1/3} . \tag{17.18}$$

Note that frequency (or wavelength) does not enter directly into Eq. (17.18), but the values of several parameters, for example, S, $\Delta\nu$, and T_S, depend upon the observing frequency. As an example, consider an observation at a frequency in the 100–300-MHz range for which we use $A = 2000$ m^2, $T_S = 200$ K, and $\Delta\nu = 2$ MHz. For an example of a radio source, we take $S = 10^{-26}$ W m^{-2} Hz^{-1} (1 Jy) and $\theta_s = 5''$. $v_{\rm m}$ is typically $0.3''$ s^{-1}. With these values, Eq. (17.18) gives $\Delta\theta = 0.7''$. Although Eq. (17.18) is derived using a geometrical optics approach, this does not limit its applicability. For an observed occultation curve, the equivalent curve for geometrical optics can be obtained by adjustment of the phases of the Fourier components.

The bandwidth of the receiving system has the effect of smearing out angular detail in an occultation observation. Thus, since the SNR increases with bandwidth, for any observation there exists a bandwidth with which the sensitivity to fine angular structure is maximized. This bandwidth is approximately $\nu^2\Delta\theta^2 R_m/c$, which can be derived from the requirement that the phase term in Eq. (17.13) not change significantly over the bandwidth. This result can be compared to the bandwidth limitation for an array [given by Eq. (6.70)] by noting that a measurement by lunar occultation with resolution $\Delta\theta$ involves examination of the wavefront, at the distance of the Moon, on a linear scale of $\lambda/\Delta\theta$. Such an interval subtends an angle $\lambda/\Delta\theta\, R_m$ at the Earth. Further discussion of such details, and of the practical implementation of Scheuer's restoration technique, is given by von Hoerner (1964), Cohen (1969), and Hazard (1976). Note that a source may undergo a number of occultations within a period of a few months, with the Moon's limb traversing the source at different position angles. If a sufficient range of position angles is observed, the one-dimensional intensity distributions can be combined to obtain a two-dimensional image of the source [see, e.g., Taylor and De Jong (1968)]. In radio astronomy, the use of lunar occultations has become less important since the development of very-long-baseline interferometry.

The method of lunar occultation has been widely used in optical and infrared astronomy to measure the size and the limb darkening of stars, and the separation of close binary stars. Consistency of the results with those of optical interferometry proves that the lunar occultation method is not corrupted by variations in the lunar topography, which can be expected to become important when the size of the variations is comparable to the Fresnel scale. Angular sizes have been routinely measured down to about 1 mas. The analysis of stellar occultation curves is usually done by fitting parameterized models, rather than the reconstruction methods used in radio observations described above. A review of special considerations for lunar occultation observations at optical and infrared wavelengths can be found in Richichi (1994). Extensive measurements of stellar diameters [see, e.g., White and

Feierman (1987)] and binary star separations [see, e.g., Evans et al. (1985)] have been made. Other applications include the measurement of subarcsecond dust shells surrounding Wolf–Rayet stars [see, e.g., Ragland and Richichi (1999)].

17.3 Measurements on Antennas

Measurement of the electric field distribution over the aperture of an antenna is an important step in optimizing the aperture efficiency, especially in the case of a reflector antenna for which such results indicate the accuracy of the surface adjustment. The Fourier transform relationship between the voltage response pattern of an antenna and the field distribution in the aperture has been derived in Sect. 15.1.2. If x and y are axes in the aperture plane, the field distribution $\mathcal{E}(x_\lambda, y_\lambda)$ is the Fourier transform of the far-field voltage radiation (reception) pattern $V_A(l, m)$ (see Sect. 3.3.1), where l and m are here the direction cosines measured with respect to the x and y axes and the subscript λ indicates measurement in wavelengths. Thus,

$$V_A(l, m) \propto \int \int_{-\infty}^{\infty} \mathcal{E}(x_\lambda, y_\lambda)\, e^{j2\pi(x_\lambda l + y_\lambda m)} dx_\lambda\, dy_\lambda \ . \tag{17.19}$$

Direct measurement of $\mathcal{E}$ can be made by moving a probe across the aperture plane, but care must be taken to avoid disturbing the field. Such a technique is useful for characterizing horn antennas for millimeter wavelengths (Chen et al. 1998). However, in many applications, especially for large antennas on fully steerable mounts, it is easier to measure V_A. It is necessary to measure both the amplitude and phase of $V_A(l, m)$ in order to perform the Fourier transform for $\mathcal{E}(x_\lambda, y_\lambda)$. To accomplish this, the beam of the antenna under test can be scanned over the direction of a distant transmitter, and a second, nonscanning, antenna can be used to receive a phase reference signal. The function $V_A(l, m)$ is obtained from the product of the signals from the two antennas. This technique resembles the use of a reference beam in optical holography, and antenna measurements of this type have been described as holographic (Napier and Bates 1973; Bennett et al. 1976).

The holographic technique is readily implemented for measurements of antennas in interferometers and synthesis arrays. If the instrumental parameters (baselines, etc.) and the source position are accurately known, and the phase fluctuations introduced by the atmosphere are negligible, then for an unresolved source, calibrated visibility values will have a real part corresponding to the flux density of the source and an imaginary part equal to zero (except for the noise). If one antenna of a correlated pair is scanned over the source, while the other antenna continues to track the source, the corresponding visibility values will be proportional to the amplitude and phase of $V_A(l, m)$ for the scanning antenna. Measurement of synthesis

array antennas as outlined above was first described by Scott and Ryle (1977), whose analysis, and that of D'Addario (1982), we largely follow below.

It is convenient to visualize the data in the aperture plane $\mathcal{E}(x_\lambda, y_\lambda)$ and in the sky plane $V_A(l, m)$ as discrete measurements at grid points in two $N \times N$ arrays to be used in the discrete Fourier transformation. For simplicity, consider a square antenna aperture with dimensions $d_\lambda \times d_\lambda$. Since $\mathcal{E}(x_\lambda, y_\lambda)$ is zero outside a range $\pm d_\lambda/2$, the sampling theorem of Fourier transforms indicates that the response must be sampled at intervals in (l, m) no greater than $1/d_\lambda$. [This interval is twice the sampling interval for the power beam because the power beam is the Fourier transform of the autocorrelation function of $\mathcal{E}(x_\lambda, y_\lambda)$.] If the $V_A(l, m)$ samples are spaced at $1/d_\lambda$, the aperture data just fill the $\mathcal{E}(x_\lambda, y_\lambda)$ array. The spacing of the measurements in the aperture is d_λ/N. Therefore, N is usually chosen so that the sample interval provides several measurements on each surface panel. In the (l, m) plane, the range of angles over which the scanning takes place is N times the pointing interval, that is, N/d_λ. This scan range is approximately N beamwidths. The procedure is to scan with the antenna under test in N^2 discrete pointing steps and thereby obtain the $V_A(l, m)$ data.

As a measure of the strength of the signal, let $\mathcal{R}_{\text{sn}}$ be the SNR obtained in time τ_a with the beams of both antennas pointed directly at the source. Now suppose that the (x_λ, y_λ) aperture plane is divided into square cells (as in Fig. 5.3) with sides d_λ/N centered on the measurement points. Consider the contribution to the correlator output of the signal from one such aperture cell, of area $(d_\lambda/N)^2$, in the antenna under test. The effective beamwidth of such an aperture cell is N times the antenna beamwidth, that is, approximately the total scan width required. Such an area contributes a fraction $1/N^2$ to the signal at the correlator output, so relative to the noise at the correlator output, the component resulting from one aperture cell is $\mathcal{R}_{\text{sn}}/N^2$ in time τ_a, or $\mathcal{R}_{\text{sn}}/N$ in time $N^2\tau_a$, which is the total measurement time. The accuracy of the phase measurement for the signal component from one aperture cell, $\delta\phi$, is the reciprocal of $\sqrt{2}$ times the corresponding SNR, that is, $N/(\sqrt{2}\mathcal{R}_{\text{sn}})$. The factor $\sqrt{2}$ is introduced because only the component of the system noise that is normal to the signal (visibility) vector introduces error in the phase measurement; see Fig. 6.8. Now a displacement ϵ in the surface of the aperture cell causes a change of phase $4\pi\epsilon/\lambda$ in the reflected signal. Thus, an uncertainty $\delta\phi$ in the phase of this signal component results in an uncertainty in ϵ of $\delta\epsilon = \lambda\delta\phi/(4\pi) = \lambda N/(4\sqrt{2}\pi\mathcal{R}_{\text{sn}})$. From the accuracy $\delta\epsilon$ desired for the surface measurement, we determine that the signal strength should be such that the SNR in time τ_a, with both beams on source, is

$$\mathcal{R}_{\text{sn}} = \frac{N\lambda}{4\sqrt{2}\pi\delta\epsilon} \,. \tag{17.20}$$

Having determined $\mathcal{R}_{\text{sn}}$, we can use Eqs. (6.48) and (6.49) to obtain values of antenna temperature or flux density (W m^{-2} Hz^{-1}) for the signal. If the two

antennas used are not of the same size, then in Eqs. (6.48) and (6.49), A, T_A, and T_S are replaced by the geometric means of the corresponding quantities. Several simplifying approximations have been made. The statement that one aperture cell contributes $1/N^2$ of the antenna output implies the assumption that the field strength is uniform over the aperture. If the aperture illumination is tapered, a higher value of $\mathcal{R}_{\text{sn}}$ will be required to maintain the accuracy at the outer edges. Consideration of a square antenna overestimates $\mathcal{R}_{\text{sn}}$ for a circular aperture of diameter d_λ by $4/\pi$. The situation can be significantly different when the signal used in the holography measurement is a cw (continuous wave) tone, for example, from a satellite. The received signal power P can be large compared with the receiver noise $kT_R\Delta\nu$ (D'Addario 1982). In that case, the noise in the correlator output is dominated by the cross products formed by the signal and the receiver noise voltages. The resulting SNR in time τ is $\sqrt{P\Delta\nu\,\tau/(kT_R\Delta\nu)}$, which is independent of the receiver bandwidth.

An example of holographic measurements on an antenna of a submillimeter-wavelength synthesis array is shown in Fig. 17.5. Some practical points are listed below.

- The source used in a holographic measurement is ideally strong enough to allow a high SNR to be obtained. Usually, either a signal from a transmitter on a satellite or a cosmic maser source is used. Morris et al. (1988) describe measurements on the 30-m-diameter antenna at Pico de Veleta in which a measurement accuracy (repeatability) of 25 μm was achieved using the 22.235-GHz water maser in Orion. For holography with interferometer elements, sources that are partially resolved can be used (Serabyn et al. 1991).
- If the test antenna is on an altazimuth mount, the beam will rotate relative to the sky as the observation proceeds. In determining the pointing directions, the (l, m) axes of the sky plane should remain aligned with the local horizontal and vertical directions. If the antenna is on an equatorial mount, the (l, m) axes should be the directions of east and north on the sky plane [i.e., the usual (l, m) definition].
- If the source is strongly linearly polarized and the antennas are on altazimuth mounts, it may be necessary to compensate for rotation of the beam. This is possible if the antennas receive on two orthogonal polarizations.
- When using two separate antennas, differences in the signal paths resulting from tropospheric irregularities can cause phase errors. It may be necessary to make periodic recordings with both beams centered on the source to determine the magnitude of such effects. In the case of measurement on a single large antenna, a small antenna mounted on the feed support structure of the large one, and pointing in the same direction as the large antenna's beam, is sometimes used to provide the on-source reference signal. Tropospheric effects on the phase should then cancel.

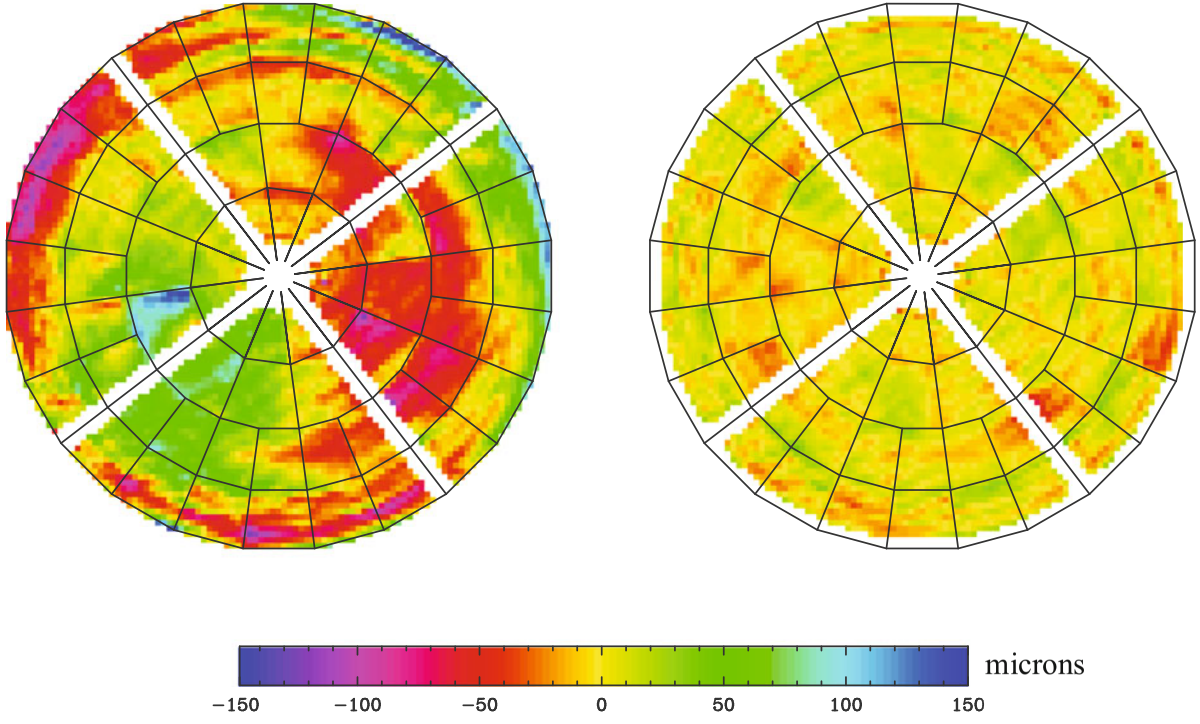

Fig. 17.5 Surface deviations of one of the 6-m-diameter antennas of the Submillimeter Array measured with holography. There are 64 panels in the reflector, which are shown by the black lines. (**left**) The surface error map when the antenna's reflector was first deployed, with an rms deviation of 65 microns. (**right**) The error map after four rounds of adjustments were completed, which achieved an accuracy of 12 microns. The expected aperture efficiency with uniform illumination at 0.5 mm [see Eq. (5.4)] is 0.91. The near-field holography measurements were carried out using a 232.4-GHz cw tone from a beacon at a distance of 219 m and standard SMA science receivers. The maps have 128 × 128 pixels and a resolution of 6 cm. Adapted from Sridharan et al. (2004).

- An antenna may be rotated (through a limited angular range) about any axis through its phase center without varying the phase of the received signal. The phase center of a parabolic reflector lies on the axis of the paraboloid and is roughly near the midpoint between the vertex and the aperture plane.[1] In the scanning, the maximum angle through which the antenna is turned from the on-source direction is $N/(2d_\lambda)$. If the axis about which it is turned is a distance r from the phase center, the phase path length to the antenna will be increased by $r[1 - \cos(N/2d_\lambda)]$. If this distance is a significant fraction of a wavelength, a phase correction must be applied to the signal at the correlator output.
- For an antenna in a radome, structural members of which can cause scattering of the incident radiation, corrections are necessary. Rogers et al. (1993) describe such corrections for measurements on the Haystack 37-m-diameter antenna.
- In measurements on the antennas of a correlator array in which the number of antennas n_a is large, a possible procedure would be to use one antenna to track the source and provide the reference signal and to scan all the others over the source. However, a better procedure would be to use $n_a/2$ antennas to track the source while the other $n_a/2$ antennas are scanned. The averaging time would be half that of the first procedure to allow the roles of the two sets of antennas to be interchanged at the midpoint of the observation. However, there would be $n_a/2$ different measurements for each antenna, so compared with the first procedure, the sensitivity would be increased by a factor $\sqrt{n_a/4}$. Also, cross-correlation of the signals from the tracking antennas would provide information about the phase stability of the atmosphere, which would be useful in interpreting the measurements.

A method that requires only measurement of the amplitude of the far-field pattern has been developed by Morris (1985). In such a procedure the reference antenna is not required. The method is based on the Misell algorithm (Misell 1973), and the procedure can be outlined as follows. Input requirements are an initial "first guess" model of the amplitude and phase of the field distribution across the antenna aperture, and two measurements of the far-field amplitude pattern, one with the antenna correctly focused and the other with the antenna defocused sufficiently to produce phase errors of a few radians at the antenna edge. The model aperture distribution is used to calculate the in-focus far-field pattern in amplitude and phase, and the calculated in-focus amplitude is replaced by the measured amplitude. The measured in-focus amplitude and the calculated phase are then used to calculate

[1] Consider transmission from an antenna in which the parabolic surface is formed by rotation of the parabola $x = ay^2$ around the x axis. Radiation from a ring-shaped element of the surface between the planes $x = x'$ and $x = x' + dx$ has an effective phase center on the x axis at x'. The area of such an element projected onto the aperture plane (i.e., normal to the x axis) is independent of x'. If the aperture illumination is uniform, each surface element between planes normal to the x axis and separated by the same increment makes an equal contribution to the electric vector in the far field. Thus, the effective phase center of the total radiation should be on the x axis, midway between the vertex and the aperture plane. Note that this is an approximate analysis based on geometrical optics.

the corresponding aperture amplitude and phase, which then become the new aperture model. This new model is then used to calculate the defocused far-field pattern. In calculating the defocused pattern, it is assumed that in the aperture, the defocusing affects only the phase and that it introduces a component that varies in the aperture as the radius squared. The calculated defocused amplitude pattern is then replaced by the measured defocused pattern, and the corresponding in-focus aperture distribution is calculated and becomes the new model. In the continuing iterations, the in-phase and defocused amplitudes are calculated alternately. After each calculation, the amplitude pattern is replaced by the corresponding measured pattern, and the result is used to upgrade the model. The required solution to which the procedure should converge is a model that fits both the in-focus and defocused responses. This technique requires a higher SNR than when phase measurements are made. For measurements near nulls in the beam, the required SNR is approximately equal to the square of that when the phase is measured (Morris 1985).

A holographic method involving only one antenna, suitable for a large submillimeter-wavelength telescope, is described by Serabyn et al. (1991). Measurements are made in the focal plane using a shearing interferometer, an adaptation of a technique used for optical instruments.

17.4 Detection and Tracking of Space Debris

Tracking of satellites and space debris by reception of scattered broadcast signals (called "noncooperative transmitters") is known as passive radar. The technique generally requires a large separation between transmitter and receiver to avoid RFI generated by receipt of the direct transmission from the transmitter. The scattering cross section for a sphere of radius a is approximately

$$\begin{aligned} \sigma &= \pi a^2 && \lambda \ll 2\pi a \,, \\ \sigma &\simeq \beta \pi a^2 \left(\frac{a}{\lambda}\right)^4 && \lambda \gg 2\pi a \,, \end{aligned} \tag{17.21}$$

where $\beta \sim 10^4$. The short wavelength limit is called geometrical scattering, and the long wavelength limit is called Rayleigh scattering. These two limits are part of the general theory of Mie scattering [see, e.g., Jackson (1998)]. The cross section of dielectric spheres scales with a and λ in the same way. Equation (17.21) shows that $\sigma/(\pi a^2)$ decreases as $(a/\lambda)^4$, so there is a sharp decrease in sensitivity for scatters smaller than $\sim \lambda$. The tracking of satellites and space debris is an important part of space situational awareness.

The use of radio arrays to passively track space objects has been demonstrated by Tingay et al. (2013) with the Murchison Widefield Array (MWA). The MWA, which operates in the 80–300 MHz frequency range, is located in Western Australia, a region of low population density and radio-quiet environment. The antennas are

dipoles mounted at ground level, which is helpful in shielding from direct reception of broadcast signals in the 87.5–108 MHz FM band. The FM signals originate from the area several hundred kilometers distant from Perth in southwestern Australia and, after scattering from objects in space, have been detected by the MWA. The directions of the incoming signals can be measured by the array, and as a test of the ability to track individual objects in space, reflections from the International Space Station were detected.

For this exercise, the astronomical interferometric delay model was adapted in an ad hoc fashion. Calculations based on Eq. (17.21) indicate that for a radius greater than 0.5 m, an object could plausibly be expected to be detected up to altitudes of approximately 1,000 km. The large collecting area of the MWA is helpful for such observations. At the FM-band frequencies, the field of view of the MWA is $\sim 2,400$ sq. deg., and the beamwidth is ~ 6 arcmin. It is estimated that on average, ~ 50 meter-size pieces of debris will be present within the MWA field of view at any time. Most will be at distances between the near-field and far-field distances for meter-wavelength observation.

A related application of radio interferometry is the near-field three-dimensional positioning of active satellites with VLBI arrays, which is described in Sect. 9.11.

17.5 Earth Remote Sensing by Interferometry

Global radio measurements have been made of the Earth since the beginning of the satellite era. For these measurements, the basic principle is that, in the absence of radiative transfer effects, the brightness temperature is related to the physical temperature of the surface through the emissivity e,

$$T_B = eT \; . \tag{17.22}$$

Since the emissivity of a material is related to its dielectric constant, the properties of the Earth's surface—e.g., moisture content of soil, salinity of sea water, and the structure of ice in the polar regions—can be deduced from maps of T_B. To obtain sufficient resolution at radio wavelengths, relatively large apertures are needed. In 2009, the European Space Agency launched the Soil Moisture and Ocean Salinity (SMOS) mission (McMullan et al. 2008; Kerr et al. 2010). This instrument strongly resembles a miniature version of the VLA. It has 69 antennas in a Y configuration (see Fig. 17.6). The system operates in the protected band of 1420–1427 MHz, which turns out to be an excellent frequency range to determine soil parameters and ocean salinity. The arm lengths are about 4 m, and the satellite is in a circular orbit with a height of 758 km and a period of 1.7 h. The maximum resolution is $\sim 2.6°$, corresponding to a linear resolution of about 35 km. The instantaneous field of view is about 1100 km. The (u, v) plane is sampled every 1.2 s. Most points on the Earth are revisited every three days. The theory of image formulation is a modified version of that presented in this book (Anterrieu 2004; Corbella et al. 2004).

Fig. 17.6 Artist's conception of the SMOS satellite, a downward-looking interferometric array operating at 21-cm wavelength and imaging the Earth at a resolution of 35 km. The length of each of the three arms of the array is 4 m, and the array is tilted by 32° to the tangent plane of the Earth below it. Image courtesy of and © European Space Agency.

The recovery of soil properties from the brightness temperature is a complex endeavor. The first step in the recovery process is based on a dielectric mixing model (Dobson et al. 1985) and the Fresnel reflection laws giving the relation between the emissivity and the dielectric constant of a surface material. A plane wave in free space incident on a flat surface with a dielectric constant ε at an incidence angle α will have power reflection coefficients of

$$r_{\parallel} = \left[\frac{\varepsilon \cos\alpha - \sqrt{\varepsilon - \sin^2\alpha}}{\varepsilon \cos\alpha + \sqrt{\varepsilon - \sin^2\alpha}} \right]^2$$

$$r_{\perp} = \left[\frac{\cos\alpha - \sqrt{\varepsilon - \sin^2\alpha}}{\cos\alpha + \sqrt{\varepsilon - \sin^2\alpha}} \right]^2 , \tag{17.23}$$

where $r_{\parallel}$ is for the electric vector component in the plane of propagation and $r_{\perp}$ is for the component normal to the plane. These are the Fresnel reflection coefficients (note that the index of refraction is $\sqrt{\varepsilon}$). The emissivity, as a function of incidence angle, is

$$e(\alpha) = 1 - r(\alpha) \; . \tag{17.24}$$

The emissivity goes to unity for $r_\parallel$ at the Brewster angle α_B,[2] given by

$$\tan \alpha_B = \sqrt{\varepsilon} \, . \tag{17.25}$$

In the case of normal incidence ($\alpha = 0$), the emissivity is

$$e_n = 1 - \left[\frac{\sqrt{\varepsilon} - 1}{\sqrt{\varepsilon} + 1} \right]^2 \, . \tag{17.26}$$

The values of ε for various types of soils and water saturation vary from about 2 to 50, corresponding to a range of e_n from 0.5 to 0.97 and a brightness temperature range, for a nominal surface temperature of 280 K, of 140 to 270 K.[3]

The actual retrieval of soil moisture requires careful modeling of the surface temperature, subsurface temperature gradient, surface roughness, and radiative transfer through the vegetation layer using a physical based algorithm (Kerr et al. 2012) or statistical methods such as neural networks (Rodríguez-Fernández et al. 2015). An example of a soil moisture map is shown in Fig. 17.7. The nominal accuracy for the technique is 4% in volumetric moisture content. The dielectric constant of sea water is ~ 80, so the ocean brightness temperature is usually below 100 K. Retrieval of ocean salinity is challenging, and even the reflection of the galactic emission on the ocean surface needs to be taken into account for accurate determinations (Font et al. 2012).

17.6 Optical Interferometry

The principles of optical interferometry are essentially identical to those at radio frequencies, but accurate measurements are more difficult to make at optical wavelengths. One difficulty arises because irregularities in the atmosphere introduce variations in the effective path length that are large compared with the wavelength and thus cause the phase to vary irregularly by many rotations. Also, obtaining the mechanical stability of an instrument required to obtain fringes at a wavelength of order 0.5 μm presents a formidable problem. However, the practicality of synthesis imaging in the optical spectrum has been demonstrated using phase closure techniques, see, e.g., Haniff et al. (1987) and Baldwin et al. (1996). In the absence of visibility phase, the amplitude data can be interpreted in terms of the autocorrelation of the intensity distribution, as explained in Sect. 11.3.3, or

[2] Clark and Kuz'min (1965) used the Owens Valley interferometer to make the first passive measurement of the dielectric constant of the surface of Venus ($\varepsilon = 2.2 \pm 0.2$) by effectively measuring the Brewster angle.

[3] The dielectric constant of sea water is ~ 80, so the ocean brightness temperature is usually below 100 K.

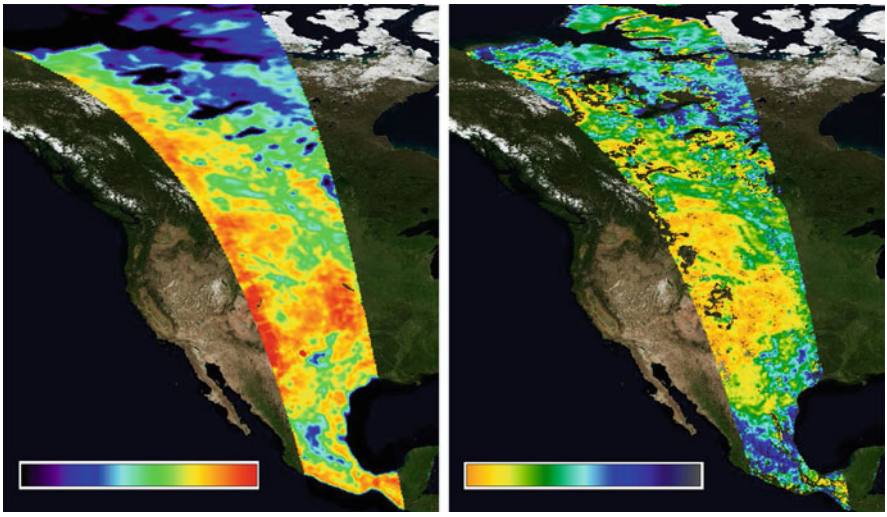

Fig. 17.7 Observations of the Earth made with the European Space Agency's SMOS orbiting synthesis array from data taken on 1 July 2015, overlaid on a visual image. (**left**) A "swath" map constructed from many snapshot images of brightness temperature in one polarization at a fixed incidence angle of 42.5°. The range of the color bar is 180–290 K. (**right**) Reconstructed map of the soil moisture based on complex retrieval algorithms and observations of each location with multiple angles of incidence and two polarizations. The range of the color bar is 0–0.5 m^3/m^3 (fractional volume). The brown shading indicates areas where the soil moisture value was not accurately retrieved. Images courtesy of Nemesio Rodríguez-Fernández and Arnaud Mialon.

in terms of models of the intensity distribution. Techniques for two-dimensional reconstruction without phase data [see, e.g., Bates (1984)] are also applicable. Optical interferometry is an active and growing field, and here we attempt only to give an overview of some basic principles. See Further Reading at the end of this chapter for a collection of important publications in optical interferometry.

Before discussing instruments, we briefly review some relevant atmospheric parameters. The irregularities in the atmosphere give rise to random variations in the refractive index over a large range of linear scales. For any particular wavelength, there exists a scale size over which portions of a wavefront remain substantially plane compared with the wavelength, that is, atmospheric phase variations are small compared with 2π. This scale size is represented by a parameter, the Fried length d_f (Fried 1966); see the discussion following Eq. (13.102). The Fried length is equal to $3.2d_0$, where d_0 is the spacing between paths through the atmosphere for which the rms phase difference is one radian; see Eq. (13.102). Regions for which the uniformity of the phase path lies within this range are sometimes referred to as seeing cells. The scale size d_f and the height at which the dominant irregularities occur define an isoplanatic angle (or isoplanatic patch) size, that is, an angular range of the sky within which the incoming wavefronts from different points encounter similar phase shifts. Within an isoplanatic patch, the point-spread function remains

Table 17.1 Atmospheric and instrumental parameters at visible and infrared wavelengths

Wavelength (μm)	d_f (m)	Isoplanatic Angle at Zenith	Resolution of 1-m-diameter aperture	Atmospheric resolution (λ/d_f)
0.5 (visible)	0.14	$5.5''$	$0.13''$	$0.70''$
2.2 (near infrared)	0.83	$33''$	$0.55''$	$0.55''$
20 (far infrared)	11.7	$8'$	$5.0''$	$0.35''$

Updated from Woolf (1982).

constant, so the convolution relationship between source and image holds. Typical figures for the 50th percentile value of d_f, which scales as $\lambda^{6/5}$ [see Eq. (13.102)], and the isoplanatic angle are given in Table 17.1. Also included for comparison are the corresponding values of the diffraction-limited resolution of a telescope of 1-m-diameter aperture. Optical interferometers provide a powerful means of studying the structure functions of the atmosphere at infrared and optical wavelengths; see, for example, Bester et al. (1992) and Davis et al. (1995). Note that techniques involving correction of atmospheric distortion of the wavefront by means of the telescope hardware are referred to as adaptive optics [see, e.g., Roggemann et al. (1997) and Milonni (1999)]. Most large telescopes have adaptive optics systems. Such systems are strongly analogous to the techniques of self-calibration and phase referencing in radio astronomy.

17.6.1 Instruments and Their Usage

The use of interferometry for measurement of the angular sizes of stars was suggested by Fizeau (1868), and the earliest attempted measurements of this type are those of Stéphan (1874), using a mask with two apertures on the objective lens of a telescope. Unfortunately, Stéphan's telescope was not large enough to resolve any of the stars he observed. The first successful measurement of the diameter of a star was made by Michelson and Pease (1921) on the supergiant star Betelgeuse, as described in Sect. 1.3.2. For this measurement, four plane mirrors were mounted on a beam attached to the telescope, so that signals received with a baseline spacing of 6 m were reflected into the telescope objective to form fringes. In this type of measurement, the whole instrument was carried on the mounting of the telescope, which simplified the pointing. However, attempts to use a similar system with an increased spacing between the mirrors were generally unsuccessful, because of the extreme stability required to maintain the relative positions of the mirrors to an accuracy of a few tenths of the optical wavelength. Thus, little progress was made in optical interferometry until the development of modern electronics and computer control for positioning of instrumental components. This allows longer baselines to be used but has become possible only in recent decades.

Figure 17.8 illustrates some of the basic features of a modern optical interferometer. The two mirrors S are mounted as siderostats and track the optical source under

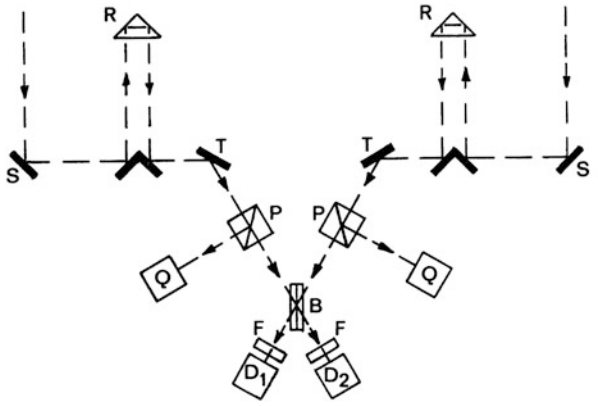

Fig. 17.8 Basic features of an optical interferometer. The broken line represents the light path from a star. From Davis and Tango (1985). With permission from and © W. J. Tango.

study. The positions of the retroreflectors R are continuously adjusted to equalize the lengths of the paths from the source to the combination point B. This delay compensation is usually implemented in evacuated tubes because the geometric delay of the interferometer largely occurs above the atmosphere. If air delay lines were used, a separate mechanism would be needed to compensate for the dispersive component of the delay, which is difficult to implement in wide bandwidth systems [see, e.g., Benson et al. (1997)]. The siderostats are mounted on stable foundations, and the rest of the system is usually mounted on optical benches within a controlled environment. The apertures of the interferometer, determined by the mirrors S, are made no larger than the Fried length d_f. Thus, the wavefront across the mirror remains essentially plane, and the effect of the irregularities is to produce a variation in the angle of arrival of the wavefront. The variation cannot be tolerated since the angles of the beams at the combination point B must be correct to within $1''$. To mitigate this effect, the polarizing beamsplitter cubes P reflect light to quadrant detectors Q, which produce a voltage proportional to any displacement of the angle of the light beam. These voltages are then used to control the tilt angles of the mirrors T, to compensate for the wavefront variation. A servo loop with bandwidth ~ 1 kHz is required to follow the fastest atmospheric effects. The filters F define the operating wavelength. The two detectors D_1 and D_2 respond to points on the fringe pattern spaced by one-quarter of a fringe cycle, and their outputs provide a measure of the instantaneous amplitude and phase of the fringes. This method is described, for example, by Rogstad (1968), who has also pointed out that with a multielement system, the phase information can be utilized by means of closure relationships, as introduced in Sect. 10.3. The system in Fig. 17.8 is shown to illustrate some of the important features used in modern optical interferometers. In practice, the siderostat mirrors may be replaced by large-aperture telescopes, and the paths of the light to the point at which the fringes are formed may be considerably more complicated.

Optical interferometers can be built with very wide bandwidths, that is, $\Delta\lambda/\lambda \simeq 0.1$ or possibly more, so the central, or white light, fringe is readily identifiable. If such a system is made to operate at two such wide wavelength bands simultaneously, the effects of the atmosphere, which is slightly dispersive, can be removed. Ground-based optical astrometry with dual-wavelength phase-tracking interferometers can yield accurate positions of stars (Colavita et al. 1987, 1999). As examples of earlier interferometry, Currie et al. (1974)) made measurements using two apertures on a single large telescope, and Labeyrie (1975) obtained the first successful measurements using two telescopes. For descriptions of later, more complex instruments, see, for example, Davis and Tango (1985); Shao et al. (1988); Baldwin et al. (1994); Mourard et al. (1994); Armstrong et al. (1998, 2013); Davis et al. (1999a,b); ten Brummelaar et al. (2005); and Jankov (2010).

For use in space where the Earth's atmosphere is avoided, optical interferometry holds great promise. The Space Interferometry Mission (SIM) (Shao 1998; Allen and Böker 1998; Böker and Allen 1999) was a space-based interferometer for the wavelength band 0.4–1.0 μm with variable baseline up to 10 m, intended to provide synthesis imaging with a resolution of 10 mas, and to measure fringe phases with sufficient accuracy to provide positions of stars to within 4 μas. It was never launched. An application of space interferometry to the detection of planets around distant stars is discussed by Bracewell and MacPhie (1979). The ratio of the signal from the planet to that from the star is maximized by choosing an infrared wavelength on the long-wavelength side of 20 μm and by placing a fringe-pattern null in the direction of the star. A demonstration of the nulling technique using ground-based telescopes is described by Hinz et al. (1998).

Rogstad (1968) describes a technique for measurement of the visibility phase using an interferometer in the presence of an atmospheric component of seeing (refraction). Consider a linear arrangement of mirrors (i.e., the optical receivers) in which a unit spacing occurs twice and all integral multiples of the unit spacing, up to a maximum value, occur at least once. The receivers are designed to measure both the amplitude and the phase of the visibility function. The phase of the visibility for each of these spacings can be derived from the measured phases plus a unit-spacing phase component. This unit-spacing phase contains a component due to the atmosphere, although the longer spacing values are free from the atmospheric effect. However, the unit-spacing phase affects only the position of the resulting image, i.e., the coordinates on the sky, and it can be set to zero without affecting the form of the image. This method has been implemented on several interferometers [e.g., Jorgensen et al. (2012)], where it is referred to as baseline bootstrapping.

Several optical interferometers have been constructed from large telescopes that are used independently part of the time. For example, the Keck Observatory on Mauna Kea has two 10-m-diameter telescopes with a spacing of 85 m. As an interferometer, these antennas can provide an effective angular resolution of 5 mas at 2.2-μm wavelength and 24 mas at 10-μm wavelength. The European Southern Observatory in Chile has constructed the Very Large Telescope Interferometer (VLTI), which consists of four 8.2-m-diameter telescopes and four auxiliary 1.8-m-diameter telescopes. With current instrumentation [Petrov et al. (2007) and

Le Bouquin et al. (2011)], up to six baselines can be correlated at once, providing multiple phase closures and imaging capability. Operating in the bands between 1.5- and 2.4-μm, resolution as fine as 2 mas can be achieved on baselines up to 130 m. Spectral line capability is also provided with $\lambda/\Delta\lambda = 12000$ (velocity resolution of 25 km s^{-1}).

In the systems mentioned above, the fringes are formed by combining the incoming radiation at the same wavelength as it is received, as in the classical Michelson stellar interferometer. They are therefore also referred to as *direct detection systems*. A disadvantage of arrays built in this way is that the light cannot be divided, with loss in SNR. An alternative to the direct detection system is the *heterodyne system*, in which the light from each aperture is mixed with coherent light from a central laser to produce an intermediate frequency (IF). The IF waveforms are then amplified and correlated in an electronic system, in a manner basically identical to that used in radio interferometry. In comparison with a direct detection system, the sensitivity is greatly limited by the quantum effects mentioned in Sect. 1.4. It is also limited by the bandwidth that can be handled by the electronic amplifiers, unless the mixer outputs are split into many frequency channels, each of which is processed in parallel. A large bandwidth can then be processed using a correspondingly large number of amplifiers and correlators. The bandwidth division also has the effect of increasing the path length difference over which the signals remain coherent. The heterodyne technique has been used in infrared interferometry; see, for example, Johnson et al. (1974), Assus et al. (1979), and Bester et al. (1990). Possible application to large multielement telescopes with multiband processing in the infrared and visible ranges has been discussed by Swenson et al. (1986).

From the submillimeter radio range to the optical is a factor of $\sim 10^3$ in wavelength, and a further factor of $\sim 10^3$ takes one to the X-ray region. X-ray astronomy could benefit greatly by the potentially high angular resolution obtainable through interferometry. The viability of X-ray interferometry, suitable for astronomical imaging, has been demonstrated in the laboratory by Cash et al. (2000). It holds the promise of providing extremely high angular resolution in observations above the atmosphere. At a wavelength of 2 nm, a baseline of 1 m provides a fringe spacing of 40 μas. In the laboratory instrument, the apertures are defined by flat reflecting surfaces, which are used at grazing incidence to minimize the requirement for surface accuracy. Direct detection is the only available technique, and if the fringes are formed by simply allowing the reflected beams to converge on a detector surface, a long distance is required to obtain sufficient fringe spacing. With 400-μas angular spacing of the fringes, adjacent maxima would be separated by only 1 μm at 500-m distance. Astronomical interferometry at X-ray wavelengths will be a challenging enterprise.

17.6.2 Sensitivity of Direct Detection and Heterodyne Systems

Factors that determine the sensitivity of optical systems, such as losses due to scattering, partial reflection, and absorption, are different from corresponding effects at radio wavelengths. However, in heterodyne systems, the most important difference is the role of quantum effects. The energy of optical photons is five or more orders of magnitude greater than that of radio photons, and quantum effects are largely negligible in the radio domain at frequencies lower than $\sim$ 100 GHz. In the optical range (wavelength $\sim$ 500 μm), the frequency is of order 600 THz, and the bandwidth could be as high as 100 THz. In a typical heterodyne system in the infrared, the wavelength of 10 μm corresponds to 30 THz, and the bandwidth used is $\sim$ 3 GHz [see, e.g., Townes et al. (1998)].

In direct detection systems, the detector or photon counter does not preserve the phase of the signal, and thus the noise resulting from the uncertainty principle, discussed in Sect. 1.4, does not occur. The noise is principally shot noise resulting from the random arrival times of the signal photons. The number of photons received from a source of intensity I is

$$N = \frac{I\Omega_s A \Delta\nu}{h\nu} \ \text{(photons s}^{-1}\text{)} \ , \tag{17.27}$$

where Ω_s is the solid angle of the source (with no atmospheric blurring), A is the collecting area of the telescope, $\Delta\nu$ is the bandwidth, ν is the frequency, and h is Planck's constant. If the source is a blackbody at temperature T, the Planck formula gives

$$I = \frac{2h\nu^3}{c^2} \frac{1}{e^{h\nu/kT} - 1} \ . \tag{17.28}$$

Note that for direct detection, we are considering the signal in both polarizations. Thus, we have

$$N = \frac{2\Omega_s A \Delta\nu}{\lambda^2} \frac{1}{e^{h\nu/kT} - 1} \ \text{(photons s}^{-1}\text{)} \ . \tag{17.29}$$

The received power is

$$P = h\nu N \ . \tag{17.30}$$

The fluctuations in the power, ΔP_D, are caused by photon shot noise and therefore are proportional to $\sqrt{N}$. Thus,

$$\Delta P_D = h\nu\sqrt{N} \ . \tag{17.31}$$

ΔP_D is known as the noise equivalent power. The SNR in one second is $P/\Delta P_D = \sqrt{N}$, and therefore for an integration time τ_a, the SNR for direct detection is

$$\mathcal{R}_{\text{snD}} = \left[\left(\frac{2\Omega_s A}{\lambda^2}\right) \frac{\Delta\nu\tau_a}{e^{h\nu/kT}-1}\right]^{1/2} , \tag{17.32}$$

where the subscript D indicates direct detection. Note that $\mathcal{R}_{\text{snD}}$ is proportional to $\sqrt{A}$, because of the shot noise, rather than to A, as in the radio case.

In a heterodyne system, the noise is determined by the uncertainty principle, since the mixer is a linear device that preserves phase. The minimum noise is one photon per mode (one photon per hertz per second), as noted in the discussion following Eq. (1.15). This is equivalent to saying that the system temperature is $h\nu/k$ [see, e.g., Heffner (1962), Caves (1982)]. Hence, in a period of one second, the uncertainty in power is

$$\Delta P_H = h\nu\sqrt{\Delta\nu} . \tag{17.33}$$

The heterodyne detector responds only to the component of the radiation to which its polarization is matched, and the received power is half of that in Eq. (17.30). The SNR for a heterodyne system (indicated by subscript H) is therefore $P/(2\Delta P_H)$ in one second, and in time τ_a, it is

$$\mathcal{R}_{\text{snH}} = \left(\frac{\Omega_s A}{\lambda^2}\right) \frac{\sqrt{\Delta\nu\tau_a}}{e^{h\nu/kT}-1} . \tag{17.34}$$

Note that Eq. (17.34) reduces to the usual radio form in Eq. (1.8) when $h\nu/kT \ll 1$. In that case, $T_A = T\Omega_s A/\lambda^2$ and the minimum value of $h\nu/k$ can be used for system temperature. The ratio of SNRs for the direct detection and heterodyne systems, when parameters other than the bandwidth are the same, is

$$\frac{\mathcal{R}_{\text{snH}}}{\mathcal{R}_{\text{snD}}} \simeq \sqrt{\left(\frac{\Omega_s A}{2\lambda^2}\right) \frac{1}{e^{h\nu/kT}-1} \left(\frac{\Delta\nu_{\text{H}}}{\Delta\nu_{\text{D}}}\right)} . \tag{17.35}$$

As indicated earlier, $\sqrt{\Delta\nu_{\text{H}}/\Delta\nu_{\text{D}}}$ could be as low as $\sim 4 \times 10^{-3}$. However, for direct detection, the propagation delays through the different siderostats to the fringe-forming point must be maintained constant to ~1/10 of the reciprocal bandwidth. This requirement restricts the bandwidths that can practicably be used, especially with baselines of hundreds of meters. The heterodyne system offers simpler hardware that provides useful sensitivity at 10 μm wavelength and possibly to the next atmospheric window at 5 μm. It also allows the amplified IF signals to be split without loss in sensitivity, to provide multiple simultaneous correlations in multielement arrays. Relative advantages of the heterodyne and direct detection systems are discussed by Townes and Sutton (1981) and de Graauw and van de Stadt (1981).

17.6.3 Optical Intensity Interferometer

The use of the intensity interferometer for optical measurements on stars was demonstrated by Hanbury Brown and Twiss (1956a), shortly after the success of the radio intensity interferometer described in Sects. 1.3.7 and 17.1. At that time, the possibility of coherence between photons in different light rays from the same source was questioned, and the physical basis and consistency with quantum mechanics is explained by Hanbury Brown and Twiss (1956c) and Purcell (1956). The laboratory demonstration of the correlation of intensity fluctuations of light by Hanbury Brown and Twiss (1956b) led to the appreciation of the phenomenon of photon bunching and to the broader development of quantum statistical studies and to their application to particle beams as well as electromagnetic radiation (Henny et al. 1999).

In the optical intensity interferometer, a photomultiplier tube at the focus of each telescope mirror replaces the RF and IF stages and the detectors of the radio instrument. The photomultiplier outputs are amplified and fed to the inputs of the correlator. The optical intensity interferometer is largely insensitive to atmospheric phase fluctuations, as explained for the radio case in Sect. 17.1. The size of the light-gathering apertures is therefore unrestricted by the scale size of the irregularities. Also, it is not necessary that the reflecting mirrors produce a diffraction-limited image, and their accuracy need only be sufficient to deliver all the light to the photomultiplier cathodes. This is fortunate since the low sensitivity mentioned earlier for the radio case necessitates the use of large light-gathering areas. Hanbury Brown (1974) gave an analysis of the response of the optical instrument and showed that it is proportional to the square of the visibility modulus as in the radio case. Either a correlator or a photon coincidence counter can be used to combine the photomultiplier outputs.

The intensity interferometer constructed at Narrabri, Australia (Hanbury Brown et al. 1967; Hanbury Brown 1974), used two 6.5-m-diameter reflectors and a bandwidth of 60 MHz for the signals at the correlator inputs. The resulting limiting magnitude of +2.5 enabled measurements of 32 stars to be made. Davis (1976) has discussed the relative merits of the intensity interferometer and modern implementations of the Michelson interferometer for development of more sensitive instruments.

17.6.4 Speckle Imaging

The image of an unresolved point source observed with a telescope of which the width of the aperture is large compared with the Fried length d_f depends on the exposure time over which the image is averaged. An exposure no longer than 10 ms shows a group of bright speckles, each of which is the approximate size of the Airy disk (i.e., the diffraction-limited point-source image) of the telescope. If the

exposure is much longer, the pattern is blurred into a single patch (the "seeing" disk) of typical diameter $1''$, determined by the atmosphere. The characteristic fluctuation time of 10 ms in the optical range corresponds to the time taken for an atmospheric cell of size $d_f \simeq 0.14$ m to move past any point in the telescope aperture at a typical wind speed of 10–20 m s^{-1}. The use of sequences of short-exposure images to obtain information at the diffraction limit of a large telescope is known as speckle imaging. Speckle patterns reflect the random distribution of atmospheric irregularities over the aperture and differ from one exposure to the next on the 10-ms timescale. Reduction of many exposures is required to observe faint objects by this technique.

For the theory of the speckle response, see, for example, Dainty (1973), Bates (1982), or Goodman (1985). Here we note that the high-resolution image represented by a single speckle can be understood if one considers each speckle as resulting from several seeing cells of the wavefront, located at points distributed across the telescope aperture. These cells are the ones that present approximately equal phase shifts in the ray paths from the wavefront to the speckle image (Worden 1977). Then, by analogy with an array of antennas, the resolution corresponds to the maximum spacing of the cells, that is, it is of the order λ/d, where d is the telescope aperture. Aberrations in the reflector do not significantly degrade the speckle pattern as long as the dominant phase irregularities are those of the atmosphere. The area of the image over which the speckles are spread corresponds to λ/d_f on the sky and becomes the seeing disk in a long exposure. The seeing cells can be regarded as subapertures within the main telescope aperture, the responses of which combine with random phases in the image. The number of speckles is of the order of the number of subapertures, that is, $(d/d_f)^2$. With a large telescope ($d \sim 1$ m), this number is of the order of 50 at optical wavelengths. Also, the size of the seeing cells increases with wavelength, and in the infrared, only a few speckles appear in the image.

A rather simple image restoration technique called the "shift-and-add" algorithm can be applied to speckle images (Christou 1991). It works best when there is a point source in the field, and at infrared wavelengths where there are relatively few speckles per frame and the isoplanatic patch is relatively large (see Table 17.1). The short exposure speckle frames are aligned on their brightest speckles and summed. The point-spread function ("dirty beam"), which can be obtained from the image of a point source within the field, will have a diffraction-limited component and a much broader component composed of the fainter speckles. This step can be followed by other restoration algorithms such as CLEAN (see Sect. 11.1) to improve the image quality further [see, e.g., Eckart et al. (1994)].

When the shift-and-add algorithm is not applicable, the modulus of the visibility can be obtained by the technique of speckle interferometry, which originated with Labeyrie (1970). This procedure can be understood from the following simplified discussion. On a single image of short exposure, a number of approximately diffraction-limited speckles appear at random locations within the seeing disk. The

speckle image $I_s(l, m)$ can be described as the convolution of the actual intensity distribution $I(l, m)$ with the speckle point-spread function $\mathcal{P}(l, m)$. Thus,

$$I_s(l, m) = I(l, m) ** \mathcal{P}(l, m) \ . \tag{17.36}$$

The function $\mathcal{P}(l, m)$ is a random function that cannot be specified exactly. As a first approximation, we will assume that $\mathcal{P}(l, m)$ is the point-spread function of the telescope in the absence of atmospheric effects, $b_0(l, m)$, replicated at the position of each speckle. Thus, we can write

$$\mathcal{P}(l, m) = \sum b_0(l - l_i, m - m_i) \ , \tag{17.37}$$

where l_i and m_i are the locations of the speckles, all of which are assumed to have the same intensity. From Eqs. (17.36) and (17.37), we obtain

$$I_s(l, m) = \sum I(l, m) ** b_0(l - l_i, m - m_i) \ . \tag{17.38}$$

If the Fourier transform of $b_0(l, m)$ is $\overline{b}_0(u, v)$, then the Fourier transform of $b_0(l - l_i, m - m_i)$ is $\overline{b}_0(u, v) \exp[j2\pi(ul_i + vm_i)]$. Hence, the Fourier transform of Eq. (17.38) can be written as

$$\overline{I}_s(u, v) = \sum \mathcal{V}(u, v)\, \overline{b}_0(u, v)\, e^{j2\pi(ul_i + vm_i)} \ , \tag{17.39}$$

where $\mathcal{V}$ and $\overline{I}$ are the Fourier transforms of I and I_s, respectively. The speckle transforms $\overline{I}_s$ cannot be summed directly because of random phase factors in Eq. (17.39). To eliminate these phase factors, we calculate $|\overline{I}_s|^2$ (i.e., $\overline{I}_s\, \overline{I}_s^*$), which is

$$\begin{aligned} |\,\overline{I}_s(u, v)|^2 &= \sum_i \sum_k |\mathcal{V}(u, v)|^2 |\,\overline{b}_0(u, v)|^2\, e^{j2\pi[u(l_i - l_k) + v(m_i - m_k)]} \\ &= |\mathcal{V}(u, v)|^2 |\,\overline{b}_0(u, v)|^2 \left[N + \sum_{i \neq k} e^{j2\pi[u(l_i - l_k) + v(m_i - m_k)]} \right] \ , \end{aligned} \tag{17.40}$$

where N is the number of speckles. Since the expectation of the summation term in the second line of Eq. (17.40) is zero, the expectation of Eq. (17.40) is

$$\langle |\,\overline{I}_s(u, v)|^2 \rangle = N_0 |\mathcal{V}(u, v)|^2 |\,\overline{b}_0(u, v)|^2 \ , \tag{17.41}$$

where N_0 is the average number of speckles. Hence, the average of a series of measurements of $|I_s(u, v)|^2$, estimated from short exposures, is proportional to the squared modulus of $\mathcal{V}(u, v)$ times the squared modulus of $\overline{b}_0(u, v)$. Since $\overline{b}_0(u, v)$ is nonzero for $|u|$ and $|v| < D/\lambda$, the function $|\mathcal{V}(u, v)|^2$ can be determined over the same range of u and v, if $\overline{b}_0(u, v)$ is known. In practice, the speckles cannot be

accurately modeled by Eq. (17.37). However, we can write

$$\langle |\overline{I}_s(u,v)|^2 \rangle = |\mathcal{V}(u,v)|^2 \, \langle |\overline{\mathcal{P}}(u,v)|^2 \rangle \, , \tag{17.42}$$

where $\overline{\mathcal{P}}(u,v)$ is the Fourier transform of $\mathcal{P}(l,m)$. From Eqs. (17.41) and (17.42), $\langle |\overline{\mathcal{P}}(u,v)|^2 \rangle$ should be approximately proportional to $|\overline{b}_0(u,v)|^2$. It can be estimated by observing a point source under the same conditions as those for the source under study.

The phase information can be extracted from the speckle frames but with considerably more computational effort. Most phase-retrieval algorithms are variations of two basic methods: the Knox–Thompson, or cross-spectral, method (Knox and Thompson 1974; Knox 1976) and the bispectrum method (Lohmann et al. 1983). These methods are described in detail by Roggemann et al. (1997).

Further Reading in Optical Interferometry

Labeyrie, A., Lipson, S.G., and Nisenson, P., *An Introduction to Optical Stellar Interferometry*, Cambridge Univ. Press, Cambridge, UK (2006)

Lawson, P.R., Ed., *Selected Papers on Long Baseline Stellar Interferometry*, SPIE Milestone Ser., MS139, SPIE, Bellingham, WA (1997)

Lawson, P.R., Ed., *Principles of Long Baseline Stellar Interferometry*, Course Notes from the 1999 Michelson Summer School, Jet Propulsion Laboratory, Pasadena, CA (2000)

Léna, P.J., and Quirrenbach, A., Eds., *Interferometry in Optical Astronomy*, Proc. SPIE, **4006**, SPIE, Bellingham, WA (2000)

Reasenberg, R.D., Ed., *Astronomical Interferometry*, Proc. SPIE, **3350**, SPIE, Bellingham, WA (1998)

Robertson, J.G., and Tango, W.J., Eds., *Very High Angular Resolution Imaging*, IAU Symp. 158, Kluwer, Dordrecht, the Netherlands (1994)

Saha, S.K., *Aperture Synthesis*, Springer, New York (2011)

Shao, M., and Colavita, M.M., Long-Baseline Optical and Stellar Interferometry, *Ann. Rev. Astron. Astrophys.*, **30**, 457–498 (1992)

ten Brummelaar, T., Tuthill, P., and van Belle, G., *J. Astron. Instrum.*, Special Issue on Optical and Infrared Interferometry, **2** (2013)

References

Allen, R.J., and Böker, T., Optical Interferometry and Aperture Synthesis in Space with the Space Interferometry Mission, in *Astronomical Interferometry*, Reasenberg, R.D., Ed., Proc. SPIE, **3350**, 561–570 (1998)

Anterrieu, E., A Resolving Matrix Approach for Synthetic Aperture Imaging Radiometers, *IEEE Trans. Geosci. Remote Sensing*, **42**, 1649–1656 (2004)

Armstrong, J.T., Hutter, D.J., Baines, E.K., Benson, J.A., Bevilacqua, R.M., Buschmann, T., Clark III J.H., Ghasempour, A., Hall, J.C., Hindsley, R.B., and ten coauthors, The Navy Precision Optical Interferometer (NPOI): An Update, *J. Astron. Instrum.*, **2**, 1340002 (8pp) (2013)

Armstrong, J.T., Mozurkewich, D., Rickard, L.J., Hutter, D.J., Benson, J.A., Bowers, P.F., Elias II N.M., Hummel, C.A., Johnston, K.J., Buscher, D.F., and five coauthors, The Navy Prototype Optical Interferometer, *Astrophys. J.*, **496**, 550–571 (1998)

Assus, P., Choplin, H., Corteggiani, J.P., Cuot, E., Gay, J., Journet, A., Merlin, G., and Rabbia, Y., L'Interféromètre Infrarouge du C.E.R.G.A., *J. Opt.* (Paris), **10**, 345–350 (1979)

Baldwin, J.E., Beckett, M.G., Boysen, R.C., Burns, D., Buscher, D.F., Cox, G.C., Haniff, C.A., Mackay, C.D., Nightingale, N.S., Rogers, J., and six coauthors, The First Images from an Optical Aperture Synthesis Array: Mapping of Capella with COAST at Two Epochs, *Astron. Astrophys.*, **306**, L13–L16 (1996)

Baldwin, J.E., Boysen, R.C., Cox, G.C., Haniff, C.A., Rogers, J., Warner, P.J., Wilson, D.M.A., and Mackay, C.D., Design and Performance of COAST, *Amplitude and Intensity Spatial Interferometry. II*, Breckinridge, J.B., Ed., Proc. SPIE, **2200**, 118–128 (1994)

Bates, R.H.T., Astronomical Speckle Imaging, *Phys. Rep.*, **90**, 203–297 (1982)

Bates, R.H.T., Uniqueness of Solutions to Two-Dimensional Fourier Phase Problems for Localized and Positive Images, *Comp. Vision, Graphics, Image Process.*, **25**, 205–217 (1984)

Bennett, J. C., Anderson, A.P., and McInnes, P.A., Microwave Holographic Metrology of Large Reflector Antennas, *IEEE Trans. Antennas Propag.*, **AP-24**, 295–303 (1976)

Benson, J.A., Hutter, D.J., Elias, N.M., Bowers, P.F., Johnston, K.J., Haijian, A.R., Armstrong, J.T., Mozurkewich, D., Pauls, T.A., Rickard, L.J., and four coauthors, Multichannel Optical Aperture Synthesis Imaging of Eta 1 Ursae Majoris with the Navy Optical Prototype Interferometer, *Astron. J.*, **114**, 1221–1226 (1997)

Bester, M., Danchi, W.C., Degiacomi, C.G., Greenhill, L.J., and Townes, C.H., Atmospheric Fluctuations: Empirical Structure Functions and Projected Performance of Future Instruments, *Astrophys. J.*, **392**, 357–374 (1992)

Bester, M., Danchi, W.C., and Townes, C.H., Long Baseline Interferometer for the Mid-Infrared, *Amplitude and Intensity Spatial Interferometry*, Breckinridge, J.B., Ed., Proc. SPIE, **1237**, 40–48 (1990)

Böker, T., and Allen, R.J., Imaging and Nulling with the Space Interferometer Mission, *Astrophys. J. Suppl.*, **125**, 123–142 (1999)

Bracewell, R.N., Radio Interferometry of Discrete Sources, *Proc. IRE*, **46**, 97–105 (1958)

Bracewell, R.N., and MacPhie, R.H., Searching for Nonsolar Planets, *Icarus*, **38**, 136–147 (1979)

Carr, T.D., Lynch, M.A., Paul, M.P., Brown, G.W., May, J., Six, N.F., Robinson, V.M., and Block, W.F., Very Long Baseline Interferometry of Jupiter at 18 MHz, *Radio Sci.*, **5**, 1223–1226 (1970)

Cash, W., Shipley, A., Osterman, S., and Joy, M., Laboratory Detection of X-Ray Fringes with a Grazing-Incidence Interferometer, *Nature*, **407**, 160–162 (2000)

Caves, C.M., Quantum Limits on Noise in Linear Amplifiers, *Phys. Rev.*, **26D**, 1817–1839 (1982)

Chen, M.T., Tong, C.-Y.E., Blundell, R., Papa, D.C., and Paine, S., Receiver Beam Characterization for the SMA, in *Advanced Technology MMW, Radio, and Terahertz Telescopes*, Phillips, T.G., Ed., Proc. SPIE, **3357**, 106–113 (1998)

Christou, J.C., Infrared Speckle Imaging: Data Reduction with Application to Binary Stars, *Experimental Astron.*, **2**, 27–56 (1991)

Clark, B.G., and Kuz'min, A.D., The Measurement of the Polarization and Brightness Distribution of Venus at 10.6-cm Wavelength, *Astrophys. J.*, **142**, 23–44 (1965)

Cohen, M.H., High Resolution Observations of Radio Sources, *Ann. Rev. Astron. Astrophys.*, **7**, 619–664 (1969)

Colavita, M.M., Shao, M., and Staelin, D.H., Two-Color Method for Optical Astrometry: Theory and Preliminary Measurements with the Mark III Stellar Interferometer, *Appl. Opt.*, **26**, 4113–4122 (1987)

Colavita, M.M., Wallace, J.K., Hines, B.E., Gursel, Y., Malbet, F., Palmer, D.L., Pan, X.P., Shao, M., Yu, J.W., Boden, A.F., and seven coauthors, The Palomar Testbed Interferometer, *Astrophys. J.*, **510**, 505–521 (1999)

Corbella, I., Duffo, N., Vall-Ilossera, M., Camps, A., and Torres, F., The Visibility Function in Interferometric Aperture Synthesis Radiometry, *IEEE Trans. Geosci. Remote Sensing*, **42**, 1677–1682 (2004)

Currie, D.G., Knapp, S.L., and Liewer, K.M., Four Stellar-Diameter Measurements by a New Technique: Amplitude Interferometry, *Astrophys. J.*, **187**, 131–134 (1974)

D'Addario, L.R., Holographic Antenna Measurements: Further Technical Considerations, 12-Meter Millimeter Wave Telescope Memo 202, National Radio Astronomy Observatory (1982)

Dainty, J.C., Diffraction-Limited Imaging of Stellar Objects Using Telescopes of Low Optical Quality, *Opt. Commun.*, **7**, 129–134 (1973)

Davis, J., High-Angular-Resolution Stellar Interferometry, *Proc. Astron. Soc. Aust.*, **3**, 26–32 (1976)

Davis, J., Lawson, P.R., Booth, A.J., Tango, W.J., and Thorvaldson, E.D., Atmospheric Path Variations for Baselines Up to 80 m Measured with the Sydney University Stellar Interferometer, *Mon. Not. R. Astron. Soc.*, **273**, L53–L58 (1995)

Davis, J., and Tango, W.J., The Sydney University 11.4 m Prototype Stellar Interferometer, *Proc. Astron. Soc. Aust.*, **6**, 34–38 (1985)

Davis, J., Tango, W.J., Booth, A.J., ten Brummelaar, T.A., Minard, R.A., and Owens, S.M., The Sydney University Stellar Interferometer—I. The Instrument, *Mon. Not. R. Astron. Soc.*, **303**, 773–782 (1999a)

Davis, J., Tango, W.J., Booth, A.J., Thorvaldson, E.D., and Giovannis, J., The Sydney University Stellar Interferometer—II. Commissioning Observations and Results, *Mon. Not. R. Astron. Soc.*, **303**, 783–791 (1999b)

de Graauw, T., and van de Stadt, H., Coherent Versus Incoherent Detection for Interferometry at Infrared Wavelengths, *Proc. ESO Conf. Scientific Importance of High Angular Resolution at Infrared and Optical Wavelengths*, Ulrich, M.H., and Kjär, K., Eds., European Southern Observatory, Garching (1981)

Dobson, M.C., Ulaby, F.T., Hallikainen, M.T., and El-Rayes, M.A., Microwave Dielectric Behavior of Wet Soil—Part II: Dielectric Mixing Models, *IEEE Trans. Geosci. Remote Sensing*, **GE-23**, 35–46 (1985)

Dulk, G.A., Characteristics of Jupiter's Decametric Radio Source Measured with Arc-Second Resolution, *Astrophys. J.*, **159**, 671–684 (1970)

Eckart, A., Genzel, R., Hofmann, R., Sams, B.J., Tacconi-Garman, L.E., and Cruzalebes, P., Diffraction-Limited Near-Infrared Imaging of the Galactic Center, in *The Nuclei of Normal Galaxies*, Genzel, R., and Harris, A., Eds., Kluwer, Dordrecht, the Netherlands (1994), pp. 305–315

Eddington, A.S., Note on Major MacMahon's Paper "On the Determination of the Apparent Diameter of a Fixed Star," *Mon. Not. R. Astron. Soc.*, **69**, 178–180 (1909)

Evans, D.S., Edwards, D.A., Frueh, M., McWilliam, A., and Sandmann, W., Photoelectric Observations of Lunar Occultations. XV, *Astron. J.*, **90**, 2360–2371 (1985)

Fizeau, H., Prix Bordin: Rapport sur le concours de l'année 1867, *Comptes Rendus des Séances de L'Académie des Sciences*, **66**, 932–934 (1868)

Font, J., Boutin, J., Reul, N., Spurgeon, P., Ballabrera-Poy, J., Chuprin, A., Gabarró, C., Gourrion, J., Guimbard, S., Hénocq, C., and 17 coauthors, SMOS First Data Analysis for Sea Surface Salinity Determination, *Int. J. Remote Sensing*, **34**, 3654–3670 (2012)

Fried, D.L., Optical Resolution Through a Randomly Inhomogenious Medium for Very Long and Very Short Exposures, *J. Opt. Soc. Am.*, **56**, 1372–1379 (1966)
Goodman, J.W., *Statistical Optics*, Wiley, New York (1985), pp. 441–459
Hanbury Brown, R., *The Intensity Interferometer*, Taylor and Francis, London (1974)
Hanbury Brown, R., Davis, J., and Allen, L.R., The Stellar Interferometer at Narrabri Observatory. I, *Mon. Not. R. Astron. Soc.*, **137**, 375–392 (1967)
Hanbury Brown, R., and Twiss, R.Q., A New Type of Interferometer for Use in Radio Astronomy, *Philos. Mag.*, Ser. 7, **45**, 663–682 (1954)
Hanbury Brown, R., and Twiss, R.Q., A Test of a New Type of Stellar Interferometer on Sirius, *Nature*, **178**, 1046–1048 (1956a)
Hanbury Brown, R., and Twiss, R.Q., Correlation Between Photons in Two Coherent Light Beams, *Nature*, **177**, 27–29 (1956b)
Hanbury Brown, R., and Twiss, R.Q., A Question of Correlation Between Photons in Coherent Light Rays, *Nature*, **178**, 1447–1448 (1956c)
Haniff, C.A., Mackay, C.D., Titterington, D.J., Sivia, D., Baldwin, J.E., and Warner, P.J., The First Images from Optical Aperture Synthesis, *Nature*, **328**, 694–696 (1987)
Hazard, C., Lunar Occultation Measurements, in *Methods of Experimental Physics*, Vol. 12, Part C *(Astrophysics: Radio Observations)*, Meeks, M.L., Ed., Academic Press, New York (1976), pp. 92–117
Hazard, C., Mackey, M.B., and Shimmins, A.J., Investigation of the Radio Source 3C273 by the Method of Lunar Occultations, *Nature*, **197**, 1037–1039 (1963)
Heffner, H., The Fundamental Noise Limit of Linear Amplifiers, *Proc. IRE*, **50**, 1604–1608 (1962)
Henny, M., Oberholzer, S., Strunk, C., Heinzel, T., Ensslin, K., Holland, M., and Schönenberger, C., The Fermionic Hanbury Brown and Twiss Experiment, *Science*, **284**, 296–298 (1999)
Hinz, P.M., Angel, J.R.P., Hoffmann, W.F., McCarthy Jr. D.W., McGuire, P.C., Cheselka, M., Hora, J.L., and Woolf, N.J., Imaging Circumstellar Environments with a Nulling Interferometer, *Nature*, **395**, 251–253 (1998)
Jackson, J.D., *Classical Electrodynamics*, Wiley, New York (1998)
Jankov, S., Astronomical Optical Interferometry. 1. Methods and Instrumentation, *Serb. Astron. J.*, **181**, 1–17 (2010)
Jennison, R.C., and Das Gupta, M.K., The Measurement of the Angular Diameter of Two Intense Radio Sources, Parts I and II, *Philos. Mag.*, Ser. 8, **1**, 55–75 (1956)
Johnson, M.A., Betz, A.L., and Townes, C.H., 10-μm Heterodyne Stellar Interferometer, *Phys. Rev. Lett.*, **33**, 1617–1620 (1974)
Jorgensen, A.M., Schmitt, H.R., van Belle, G.T., Mozurkewich, D., Hutter, D., Armstrong, J.T., Baines, E.K., Restaino, S., and Hall, T., Coherent Integration in Optical Interferometry, in *Optical and Infrared Interferometry III*, Proc. SPIE, **8445**, 844519 (2012)
Kerr, Y.H., Waldteufel, P., Wigneron, J.-P., Delwart, S., Cabot, F., Boutin, J., Escorihuela, M.-J., Font, J., Reul, N., Gruhier, C., and five coauthors, The SMOS Mission: New Tool for Monitoring Key Elements of the Global Water Cycle, *Proc. IEEE*, **98**, 666–687 (2010)
Kerr, Y.H., Waldteufel, P., Richaume, P., Wigneron, J.P., Ferrazzoli, P., Mahmoodi, A., Al Bitar, A., Cabot, F., Gruhier, C., Enache Juglea, S., and three coauthors, The SMOS Soil Moisture Retrieval Algorithm, *IEEE Trans. Geosci. Remote Sensing*, **50**, 1384–1403 (2012)
Knox, K.T., Image Retrieval from Astronomical Speckle Patterns, *J. Opt. Soc. Am.*, **66**, 1236–1239 (1976)
Knox, K.T., and Thompson, B.J., Recovery of Images from Atmospherically Degraded Short-Exposure Photographs, *Astrophys. J. Lett.*, **193**, L45–L48 (1974)
Labeyrie, A., Attainment of Diffraction-Limited Resolution in Large Telescopes by Fourier Analysing Speckle Patterns in Star Images, *Astron. Astrophys.*, **6**, 85–87 (1970)
Labeyrie, A., Interference Fringes Obtained on Vega with Two Optical Telescopes, *Astrophys. J. Lett.*, **196**, L71–L75 (1975)
Le Bouquin, J.-B., Berger, J.-P., Lazareff, B., Zins, G., Haguenauer, P., Jocou, L., Kern, P., Millan-Gabet, R., Traub, W., Absil, O., and 36 coauthors, PIONIER: A Four-Telescope Visitor Instrument at VLTI, *Astron. Astrophys.*, **535**, A67 (14pp) (2011)

Lohmann, A.W., Weigelt, G., and Wirnitzer, B., Speckle Masking in Astronomy: Triple Correlation Theory and Applications, *Appl. Optics*, **22**, 4028–4037 (1983)

MacMahon, P.A., On the Determination of the Apparent Diameter of a Fixed Star, *Mon. Not. R. Astron. Soc.*, **69**, 126–127 (1909)

McMullan, K.D., Brown, M.A., Martín-Neira, M., Rits, W., Ekholm, S., Martí, J., and Lemanczyk, J., SMOS: The Payload, *IEEE Trans. Geosci. Remote Sensing*, **46**, 594–605 (2008)

Michelson, A.A., and Pease, F.G., Measurement of the Diameter of α Orionis with the Interferometer, *Astrophys. J.*, **53**, 249–259 (1921)

Milonni, P.W., Resource Letter: Orionis with the Interferometer AOA-1: Adaptive Optics in Astronomy, *Am. J. Phys.*, **67**, 476–485 (1999)

Misell, D.L., A Method for the Solution of the Phase Problem in Electron Microscopy, *J. Phys. D.*, **6**, L6–L9 (1973)

Morris, D., Phase Retrieval in the Radio Holography of Reflector Antennas and Radio Telescopes, *IEEE Trans. Antennas Propag.*, **AP-33**, 749–755 (1985)

Morris, D., Baars, J.W.M., Hein, H., Steppe, H., Thum, C., and Wohlleben, R., Radio-Holographic Reflector Measurement of the 30-m Millimeter Radio Telescope at 22 GHz with a Cosmic Signal Source, *Astron. Astrophys.*, **203**, 399–406 (1988)

Mourard, D., Tallon-Bosc, I., Blazit, A., Bonneau, D., Merlin, G., Morand, F., Vakili, F., and Labeyrie, A., The G12T Interferometer on Plateau de Calern, *Astron. Astrophys.*, **283**, 705–713 (1994)

Napier, P.J., and Bates, R.H.T., Antenna-Aperture Distributions from Holographic Type of Radiation-Pattern Measurements, *Proc. IEEE*, **120**, 30–34 (1973)

Petrov, R.G., Malbet, F., Weigelt, G., Antonelli, P., Beckmann, U., Bresson, Y., Chelli, A., Dugué, M., Duvert, G., Gennari, S., and 88 coauthors, AMBER, The Near-Infrared Spectro-Interferometric Three-Telescope VLTI Instrument, *Astron. Astrophys.*, **464**, 1–12 (2007)

Purcell, E.M., A Question of Correlation between Photons in Coherent Light Rays, *Nature*, **178**, 1449–1450 (1956)

Ragland, S., and Richichi, A., Detection of a Sub-Arcsecond Dust Shell around the Wolf–Rayet Star WR112, *Mon. Not. R. Astron. Soc.*, **302**, L13–L16 (1999)

Richichi, A., Lunar Occultations, in *Very High Angular Resolution Imaging*, IAU Symp. 158, Robertson, J.G., and Tango, W.J., Eds., Kluwer, Dordrecht, the Netherlands (1994), pp. 71–81

Rodríguez-Fernández, N.J., Aires, F., Richaume, P., Kerr, Y.H., Prigent, C., Kolassa, J., Cabot, F., Jiménez, C., Mahmoodi, A., and Drusch, M., Soil Moisture Retrieval Using Neural Networks: Application to SMOS, *IEEE Trans. Geosci. Remote Sensing*, **53**, 5991–6006 (2015)

Rogers, A.E.E., Barvainis, R., Charpentier, P.J., and Corey, B.E., Corrections for the Effect of a Radome on Antenna Surface Measurements Made by Microwave Holography, *IEEE Trans. Antennas Propag.*, **AP-41**, 77–84 (1993)

Roggemann, M.C., Welch, B.M., and Fugate, R.Q., Improving the Resolution of Ground-Based Telescopes, *Rev. Mod. Phys.*, **69**, 437–505 (1997)

Rogstad, D.H., A Technique for Measuring Visibility Phase with an Optical Interferometer in the Presence of Atmospheric Seeing, *Appl. Opt.*, **7**, 585–588 (1968)

Scheuer, P.A.G., On the Use of Lunar Occultations for Investigating the Angular Structure of Radio Sources, *Aust. J. Phys.*, **15**, 333–343 (1962)

Scott, P.F., and Ryle, M., A Rapid Method for Measuring the Figure of a Radio Telescope Reflector, *Mon. Not. R. Astron. Soc.*, **178**, 539–545 (1977)

Serabyn, E., Phillips, T.G., and Masson, C.R., Surface Figure Measurements of Radio Telescopes with a Shearing Interferometer, *Appl. Optics*, **30**, 1227–1241 (1991)

Shao, M., SIM: The Space Interferometry Mission, in *Astronomical Interferometry*, Reasenberg, R.D., Ed., Proc. SPIE, **3350**, 536–540 (1998)

Shao, M., Colavita, M., Hines, B.E., Staelin, D.H., Hutter, H.J., Johnston, K.J., Mozurkewich, D., Simon, R.S., Hershey, J.L., Hughes, J.A., and Kaplan, G.H., The Mark III Stellar Interferometer, *Astron. Astrophys.*, **193**, 357–371 (1988)

Sridharan, T.K., Saito, M., Patel, N.A., and Christensen, R.D., Holographic Surface Setting of the Submillimeter Array Antennas, in *Astronomical Structures and Mechanisms Technology*, Antebi, J., and Lemke, D., Eds., Proc. SPIE, 5495, 441–446 (2004)

Stéphan, E., Sur l'extrême petitesse du diamètre apparent des étoiles fixes, *Comptes Rendus des Séances de L'Académie des Sciences*, **78**, No. 15 (meeting of April 13, 1874), 1008–1012 (1874)

Swenson, Jr. G.W., Gardner, C.S., and Bates, R.H.T., Optical Synthesis Telescopes, in *Infrared, Adaptive, and Synthetic Aperture Optical Systems*, Proc. SPIE, **643**, 129–140 (1986)

Taylor, J.H., and De Jong, M.L., Models of Nine Radio Sources from Lunar Occultation Observations, *Astrophys. J.*, **151**, 33–42 (1968)

ten Brummelaar, T.A., McAlister, H.A., Ridgway, S.T., Bagnuolo Jr. W.G., Turner, N.H., Sturmann, L., Sturmann, J., Berger, D.H., Ogden, C.E., Cadman, R., and three coauthors, First Results from the Chara Array. II. A Description of the Instrument, *Astrophys. J.*, **628**, 453–465 (2005)

Tingay, S.J., Kaplan, D.L., McKinley, B., Briggs, F., Wayth, R.B., Hurley-Walker, N., Kennewell, J., Smith, C., Zhang, K., Arcus, W., and 53 coauthors, On the Detection and Tracking of Space Debris Using the Murchison Widefield Array: I. Simulations and Test Observations Demonstrate Feasibility, *Astron. J.*, **146**, 103–111 (2013)

Townes, C.H., Bester, M., Danchi, W.C., Hale, D.D.S., Monnier, J.D., Lipman, E.A., Tuthill, P.G., Johnson, M.A., and Walters, D., Infrared Spatial Interferometer, in *Astronomical Interferometry*, Reasonberg, R.D., Ed., Proc. SPIE, **3350**, 908–932 (1998)

Townes, C.H., and Sutton, E.C., Multiple Telescope Infrared Interferometry, *Proc. ESO Conf. on Scientific Importance of High Angular Resolution at Infrared and Optical Wavelengths*, Ulrich, M.H., and Kjär, K., Eds., European Southern Observatory, Garching (1981), pp. 199–223

von Hoerner, S., Lunar Occultations of Radio Sources, *Astrophys. J.*, **140**, 65–79 (1964)

White, N.M., and Feierman, B.H., A Catalog of Stellar Angular Diameters Measured by Lunar Occultation, *Astrophys. J.*, **94**, 751–770 (1987)

Whitford, A.E., Photoelectric Observation of Diffraction at the Moon's Limb, *Astrophys. J.*, **89**, 472–481 (1939)

Woolf, N.J., High Resolution Imaging from the Ground, *Ann. Rev. Astron. Astrophys.*, **20**, 367–398 (1982)

Worden, S.P., Astronomical Image Reconstruction, *Vistas in Astronomy*, **20**, 301–318 (1977)